

Long-Term, Continuous Monitoring of the Broad Line Radio Galaxies 3C 390.3 and 3C 120 With the Rossi X-Ray Timing Explorer

Mario Gliozzi¹, Rita M. Sambruna¹, and Michael Eracleous²

ABSTRACT

We present a study of the flux and spectral variability of the two broad-line radio galaxies (BLRGs) 3C 390.3 and 3C 120, observed almost daily with the *Rossi X-Ray Timing Explorer (RXTE)* for nearly two months each in 1996 and 1997, respectively. Our original motivation for this study was to search for systematic differences between BLRGs and their radio-quiet counterparts, the Seyfert galaxies, whose temporal and spectral behavior is better studied. We find that both 3C 390.3 and 3C 120 are highly variable, but in a different way, and quantify this difference by means of a structure function analysis. 3C 390.3 is significantly more variable than 3C 120, despite its jet larger inclination angle, implying either that the X-ray variability is not dominated by the jet or that two different variability processes are simultaneously at work in 3C 390.3. We performed an energy-selected and time-resolved analysis based on the fractional variability amplitude and found that the variability amplitude of both objects is strongly anticorrelated with the energy. This last result, along with the correlated change of the photon index with the X-ray continuum flux, can be qualitatively explained within the scenario of thermal Comptonization, generally invoked for radio-quiet active galaxies. Moreover, the time-resolved and energy-selected fractional variability analyses show a trend opposite to that observed in jet-dominated AGN (blazars), suggesting only a minor contribution of the jet to the X-ray properties of BLRGs. Time-averaged spectral analysis indicates the presence of a strong, resolved Fe K α line with centroid at 6.4 keV and a weak ($\Omega/2\pi \simeq 0.1 - 0.4$) reflection component in both objects. The overall PCA+HEXTE spectra are best fitted with the constant density ionization model of Ross & Fabian, but with

¹George Mason University, Dept. Of Physics & Astronomy, 4400 University Drive, Ms 3f3, Fairfax, Va 22030 (e-mail: mario,rms@physics.gmu.edu).

²The Pennsylvania State University, Department of Astronomy And Astrophysics, 525 Davey Lab, State College, Pa 16802 (e-mail: mce@astro.psu.edu).

a modest ionization parameter. We performed a time-resolved spectral analysis of 3C 390.3 with the aim of constraining the delay between Fe K α line and continuum variability; however, the limited signal-to-noise ratio of the line flux hampers a thorough study of the line variability.

1. Introduction

Active Galactic Nuclei (AGN) are variable in every observable waveband. The X-ray flux exhibits variability on timescales shorter than in any other energy band, indicating that the emission occurs in the innermost regions of the central engine. A fundamental open question in the study of AGN concerns the difference between radio-loud and radio-quiet objects. If, as widely believed, this difference is not related to the nature of the host galaxy, but to some intrinsic difference in the central engine (either connected to the properties of the supermassive black hole or to the nature of the accretion flow), then X-ray temporal and spectral variability can provide constraints on the physical conditions in the inner parts of the accretion flow and shed light on the radio-loudness dichotomy.

We have been carrying out a systematic study of radio-loud AGN at X-ray wavelengths (Sambruna, Eracleous, & Mushotzky 1999; Eracleous Sambruna, & Mushotzky 2000; Hasenkopf, Sambruna, & Eracleous 2002) to investigate in detail the properties of their nuclear emission and the structure of their accretion flows. While the X-ray timing properties of Seyferts are relatively well known (e.g., Nandra et al. 1997; Leighly 1999; Turner et al. 1999), in their radio-loud counterparts, the Broad-Line Radio Galaxies (BLRGs), the variability of the X-ray emission is not as well studied. We targeted two well-known BLRGs, 3C 390.3 and 3C 120, for intensive X-ray monitoring because they are among the brightest BLRGs and are known to be variable, based on previous studies with *Einstein* and *ROSAT* (Halpern 1985, Leighly & O’Brien 1997). We used *RXTE* to perform a long-term monitoring of their flux and spectral variability, since it has a unique combination of flexible scheduling, relaxed pointing constraints, high throughput, and rapid slew speed.

Previous X-ray studies with *Ginga*, *ASCA*, *RXTE*, and *BeppoSAX* (Woźniak et al. 1998, Sambruna et al. 1999, Eracleous et al. 2000, Zdziarski & Grandi 2001) show that BLRGs usually have weaker Fe K α emission lines and Compton “reflection” components than Seyfert 1s. While all the authors basically agree on these observational results, their interpretation is still a matter of debate. In particular, Woźniak et al. (1998) suggested that the reprocessing medium is located at a very large distance from the central engine and identified the obscuring torus invoked in AGN unification schemes as a plausible site. On the other hand, Eracleous et al. (2000) suggested that the reprocessing medium is the outer part of the accretion

disk, which is much closer to the central engine than in the above picture (at distances of order 10^3 gravitational radii). These authors also proposed that the central engines of BLRGs are fueled at a rate much lower than the Eddington rate, with the result that their inner accretion disks have the form of a vertically extended advection-dominated accretion flow (ADAF; see, for example, Narayan, Mahadevan, & Quataert 1998 for a review) that illuminates the outer, thin disk. The most recently suggested interpretation is by Ballantyne et al. (2002), who noted that the weakness of the X-ray reprocessing features is consistent with Compton “reflection” and fluorescence in an *ionized* accretion disk. Therefore, they proposed that the accretion disks of BLRGs are highly ionized as a consequence of a very high accretion rate, which reaches a substantial fraction of the Eddington rate. To illustrate the point these authors showed that the *ASCA* spectrum of 3C 120 can be fitted by a reprocessing model employing an ionized accretion disk.

Distinguishing among the above interpretations is important since it would help us understand the cause of the difference between radio-loud and radio-quiet AGNs. With this in mind, we investigate possible correlated variations of the Fe line and continuum flux in an attempt to constrain the location of the reprocessor, and comment on future observational tests.

The outline of the paper is as follows. In § 2 we describe the observations and data reduction. In § 3 we study the temporal and spectral variability of 3C 390.3 and 3C 120 using different techniques: the structure function to determine the characteristic time-scales of the sources; the fractional variability parameter to quantify the timing behavior in energy-selected light curves and in time-selected intervals; the hardness ratios to investigate the spectral variability. In § 4 we analyze the spectral properties of the two objects by fitting different spectral models to the time-averaged spectra and we also investigate the spectral evolution of 3C 390.3 using time-resolved spectra. In § 5 we discuss the implications of the results of the temporal and spectral analysis. Finally, in § 6 we draw the main conclusions. Throughout the paper we use a Friedman cosmology with $H_0 = 75 \text{ km s}^{-1} \text{ Mpc}^{-1}$ and $q_0 = 0.5$ for the computation of K-corrected luminosities.

2. *RXTE* Observations And Data Reduction

In Table 1 we list the basic properties of 3C 390.3 and 3C 120, namely the redshift, the inferred inclination of the radio jet (see Eracleous & Halpern 1998 and references therein) and the column density of the Galactic interstellar medium, along with the dates and times of the observations. 3C 390.3 was monitored from 1996 May 17 to July 12, with the following sampling: for the first 24 days the source was regularly observed for roughly one hour once per

day, for the subsequent 10 days the sampling density was increased to two short observations per day, then the source was again observed once per day for 14 days, finally, during the last 10 days the observations were carried out once every two days. 3C 120 was observed from 1997 January 10 to March 8, with a sampling pattern as even as possible (i.e. approximately one observation per day). The observations were carried out with the Proportional Counter Array (PCA; Jahoda et al. 1996), and the High-Energy X-Ray Timing Experiment (HEXTE; Rothschild et al. 1998) on *RXTE*.

The PCA data were screened according to the following acceptance criteria: the satellite was out of the South Atlantic Anomaly (SAA) for at least 30 min, the Earth elevation angle was $\geq 10^\circ$, the offset from the nominal optical position was $\leq 0:02$, and the parameter ELECTRON-0 was ≤ 0.1 . The last criterion removes data with high particle background rates in the Proportional Counter Units (PCUs). The PCA background spectrum and light curve were determined using the L7 – 240 model developed at the *RXTE* Guest Observer Facility (GOF) and implemented by the program `pcabackest` v.2.1b. This model is appropriate for “faint” sources, i.e., those producing count rates less than $40 \text{ s}^{-1} \text{ PCU}^{-1}$. All the above tasks were carried out using the `FTOOLS` v.5.1 software package and with the help of the `rex` script provided by the *RXTE* GOF, which also produces response matrices and effective area curves appropriate for the time of the observation. Data were initially extracted with 16 s time resolution and subsequently rebinned at different bin widths depending on the purpose for which they were employed. The current temporal analysis is restricted to PCA, STANDARD-2 mode, 2–11 keV, Layer 1 data, because that is where the PCA is best calibrated and most sensitive. Since PCUs 3 and 4 were occasionally turned off, only data from the other three PCUs (0, 1, and 2) were used. All quoted count rates are normalized to 1 PCU. For the spectral analysis, in order to increase the signal-to-noise ratio, we used data from all the available PCUs (the spectra were combined with the help of the software tool `addspect`).

The HEXTE data, used in combination with the PCA data for the spectral analysis, were also screened to exclude events recorded where the pointing offset was greater than 0.02° , and when the Earth elevation angle was less than 10° . The background in the two HEXTE clusters is measured during each observation by rocking the instrument slowly on and off source. Therefore, source and background photons are included in the same data set and are separated into source and background spectra according to the time they were recorded. Due to their low signal-to-noise ratio, HEXTE data are used only in the time-averaged spectral analysis, for the purpose of constraining the reflection component of the broad band spectrum. Average count rates of the PCA and HEXTE cluster 0, as well as exposure times, are listed in Table 2.

3. X-Ray Temporal Analysis

Figure 1 shows the background-subtracted light curves of 3C 390.3 and 3C 120 in the 2–11 keV energy range. The observed ($2.1 \text{ s}^{-1} \text{ PCU}^{-1}$) mean PCA count rate for 3C 390.3 corresponds to a 2–10 keV flux of $2.6 \times 10^{-11} \text{ erg s}^{-1} \text{ cm}^{-2}$ and a luminosity $L_{2-10} = 1.6 \times 10^{44} \text{ erg s}^{-1}$. For 3C 120 ($5.2 \text{ s}^{-1} \text{ PCU}^{-1}$), $F_{2-10} = 6.1 \times 10^{-11} \text{ erg s}^{-1} \text{ cm}^{-2}$ and $L_{2-10} = 1.3 \times 10^{44} \text{ erg s}^{-1}$. These luminosities were calculated assuming a power-law spectral model with the best fit parameters that we present later on in this paper (see Table 4). 3C 390.3 exhibits a trend of decreasing flux by a factor 2 in 20 days, with smaller changes (a few percent) on timescales of 4 days or less, superposed. 3C 120 shows erratic flux variations similar to “flickering”, with small-amplitude intra-day “flares” superposed on a roughly constant baseline. The most prominent feature in the latter light curve is the presence of a sharp dip shortly before the end of the monitoring campaign, with a count rate decrease by a factor of 50% in few days and a subsequent recovery to the previous value in one day. As a check, we analyzed separately the light curves of the source and the background for each individual PCU and concluded that the dip cannot be attributed to instrumental effects. Moreover, the presence of remarkable short-time variability in 3C 120 is not surprising: *ROSAT* observations (Grandi et al. 1997) have already shown the presence of variations of the 0.1-2 keV flux by factors larger than 1 in $\sim 8000 \text{ s}$, indicating that the region producing the photons cannot be larger than 10^{15} cm , provided that the X-ray emission is isotropic. Throughout the temporal analysis section we assume for statistical tests a level of significance of 90%, meaning that there is a chance probability of 10% that an hypothesis is erroneously rejected.

3.1. Structure Function

In order to quantify the different timing behavior of the two BLRGs, we first carried out a structure function analysis (e.g. Simonetti et al. 1985, Hughes et al. 1992). This is a method frequently used in astronomy to quantify time variability without the problems encountered in the traditional Fourier analysis technique in case of unevenly sampled data. The first-order structure function is defined as the mean deviation for data points separated by a time lag τ :

$$SF(\tau) = \langle [F(t) - F(t + \tau)]^2 \rangle \quad (1)$$

One of the most useful features of the structure function is its ability to discern the range of timescales that contribute to the variations in the data set: the characteristic timescales of the variability are identified by the maxima and slope changes in the $\tau - SF$ plane. For a

stationary random process the structure function reaches a plateau state for lags longer than the longest correlation timescale. In other words, the time at which the structure function reaches a plateau state is interpreted as the characteristic timescale of the source.

Figure 2 shows the structure functions of 3C 390.3 (top) and 3C 120 (bottom panel). While the structure function of 3C 390.3 resembles the behavior expected from an ideal stationary random process with a smooth increase until a plateau state is reached at $\sim (2 - 2.5) \times 10^6$ s (\simeq 25-30 days), the structure function of 3C 120 does not show any clear trend. This reflects the fact that 3C 390.3 showed a roughly smooth decay with a decaying timescale of the order of 25 days, while 3C 120 did not show any long term trend during the observational campaign.

3.2. Fractional Variability

A different way to quantify the variability properties of 3C 390.3 and 3C 120, without considering the time ordering of the values in the light curves, is to calculate the fractional variability parameter F_{var} (e.g. Rodriguez-Pascual et al. 1997, Edelson et al. 2002). This is a common measure of the intrinsic variability amplitude relative to the mean count rate, corrected for the effect of random errors, i.e.,

$$F_{\text{var}} = \frac{(\sigma^2 - \Delta^2)^{1/2}}{\langle r \rangle} \quad (2)$$

where σ^2 is the variance, $\langle r \rangle$ the unweighted mean count rate, and Δ^2 the mean square value of the uncertainties associated with each individual count rate.

We first computed F_{var} for the whole light curves in the 2–11 keV energy band using 5760 s (\sim one orbit) time bins, and found 26.6% and 8.5% for 3C 390.3 and 3C 120, respectively. This simply indicates that the long-term flux variability in 3C 390.3 is larger than in 3C 120, as expected from the visual inspection of the two light curves.

More interesting results are obtained by computing the fractional variability parameter on selected energy bands. For both 3C 390.3 and 3C 120 we used light curves in three energy bands, 2-5 keV (soft band), 5-7 keV (medium band) and 7-11 keV (hard band), and calculated F_{var} for all of them. All bands show significant variability. The mean count rate $\langle rate \rangle$, and the fractional variability parameter F_{var} calculated using time bins of 1440 s (\sim a quarter of an orbit) for the light curves of 3C 390.3 and 3C 120 in the soft, medium and hard band, are given in Table 3. For both objects, we found that the amplitude of variability decreases with increasing energy band, with 3C 390.3 showing a fractional variability of 31% in the soft band, and 25% in the hard band, while 3C 120 has F_{var} decreasing from 9% in the

soft band to 6.4% in the hard band. These results are displayed in Figure 3 and Figure 4, along with the light curves in each of the three energy bands.

We have carried out a χ^2 test to verify the hypothesis that the F_{var} vs energy band trend is consistent with a constant. Both sources show evidence of statistically significant variability of F_{var} vs energy: for 3C 390.3 we obtained $\chi^2 = 5.2$ for 2 degrees of freedom, with a chance probability $P_{\chi^2} \sim 7\%$; for 3C 120 $\chi^2 = 12.9$, $P_{\chi^2} \ll 1\%$.

To quantify the degree of linear correlation between F_{var} and the energy band (and all the other possible correlations thereafter), we calculate the linear correlation coefficient r and compute the chance probability $P_c(r; N)$ that a random sample of N uncorrelated pairs of measurements would yield a linear correlation coefficient equal or larger than $|r|$; if this chance probability is small, the two quantities are likely to be correlated. For 3C 390.3 we found $r = -0.999$ and $P_c \sim 2\%$, and for 3C 120 $r = -0.975$ and $P_c \sim 10\%$, which confirm the presence of an anti-correlation between F_{var} and the energy band. The results of the χ^2 test and correlation analysis are reported in Table 3.

To examine the evolution of the timing properties of 3C 390.3 and 3C 120 further, we split the two long-term light curves, binned at 5760 s, into evenly sampled sub-intervals of nearly four days for 3C 390.3 and six days for 3C 120 (even sampling is important because F_{var} depends strongly on the duration of the data-train). The reason for choosing shorter intervals for 3C 390.3 is that we want to measure the short-term variability (and its trend versus the local count rate) without the bias of the long-term variability trend. We then calculated F_{var} over each interval and found that 3C 390.3 shows no evidence for significant variability ($\chi_{\text{red}}^2 = 1.03$, $P_{\chi^2} \sim 40\%$) nor correlation between the variability and count rate ($r = -0.05$, $P_c \simeq 90\%$), while the fractional variability of 3C 120 is statistically variable ($\chi_{\text{red}}^2 = 34.9$, $P_{\chi^2} \ll 1\%$) and marginally anticorrelated with the local average count rate ($r = -0.67$, $P_c \simeq 15\%$). In any case, Figure 5 (bottom panel) shows that the flux variability parameter of 3C 120 is significantly smaller for count rate values above a certain threshold.

3.3. X-Ray Colors

X-ray colors provide a simple, model-independent way of investigating spectral variability. We defined three colors as ratios of count rates in different bands: Hard/Soft = F_{7-11}/F_{2-5} , Hard/Med = F_{7-11}/F_{5-7} , and Med/Soft = F_{5-7}/F_{2-5} . Figure 6 shows Med/Soft, Hard/Med and Hard/Soft plotted versus time for both 3C 390.3 and 3C 120. According to a χ^2 test, all the colors with the only exception of the Med/Soft color in 3C 120 exhibit statistically significant variations, with a higher variability for the Hard/Soft ratio. For the

Med/Soft color of 3C 390.3 we found $\chi^2 = 108$ corresponding to a chance probability $< 2\%$ for 81 d.o.f; $\chi^2 = 149$ and 241 (with $P_{\chi^2} \ll 1\%$ in both cases) for Hard/Med and Hard/Soft, respectively. For the Med/Soft color of 3C 120 we found $\chi^2 = 58.3$ corresponding to a chance probability of $\sim 32\%$ for 54 d.o.f; $\chi^2 = 147$ for Hard/Med and $\chi^2 = 210$ for Hard/Soft with $P_{\chi^2} \ll 1\%$ in both cases. The presence of spectral variability is also clearly demonstrated in the plots of the color against the count rate in Figure 6.

Figure 7 shows the X-ray color (F_{7-11}/F_{2-5}) of 3C 390.3 (top panel) and 3C 120 (bottom panel) plotted against the average count rate in the 2-5 keV + 7-11 keV energy band. Both sources show a strong anticorrelation between colors and count rates: the linear correlation coefficients are $r = -0.84$ for 3C 390.3 and $r = -0.59$ for 3C 120; the probability that uncorrelated data would give a linear correlation coefficient larger than the values found in either case is much smaller than 1%. With a linear least square fit we found the following slopes: $(-19.8 \pm 1.9) \times 10^{-2}$ for 3C 390.3 and $(-1.4 \pm 0.3) \times 10^{-2}$ for 3C 120.

Having selected three continuum energy bands, we can also construct color-color diagrams. The main purposes for this analysis is to show: 1) that the two sources, similar in many aspects, behave differently, as already pointed out by the structure function analysis, and, more importantly, 2) that 3C 390.3 show a distinct bimodal behavior during the monitoring campaign (see text below). Figure 8 shows the color-color plots of 3C 390.3 (top panel) and 3C 120 (bottom panel). While in the latter the points are crowded in the central region with evidence for a weak positive correlation ($r = 0.32$, $P_c \simeq 3\%$), the color-color diagram of 3C 390.3 looks more complex. To investigate the possible correspondence of the positions in the color-color plot with the evolution of the light curve, we have plotted with filled dots the values corresponding to the first half of the light curve (i.e. during the smooth decay phase) and with open diamonds the values corresponding to the second half of the light curve (i.e. during the phase of nearly stationary flux). The color-color plot clearly indicates the presence of a bimodal trend: during the decay phase of the light curve the points are positively correlated ($r = 0.51$, $P_c = 2\%$), while during the stationary phase there is a strong inverse correlation ($r = -0.72$, $P_c \ll 1\%$) between Hard/Med and Med/Soft. In fact the behavior of 3C 390.3 in color-color space is reminiscent of the Z-shaped tracks of some low-mass X-ray binaries (the “Z sources”; Hasinger & van der Klis 1989; see also van der Klis 1995 for a recent review). In the case of 3C 390.3, not all three branches of the Z-shaped track are traced, only the horizontal and normal branches.

4. Spectral Analysis

The presence of pronounced spectral variability, as shown by the color analysis in the previous section for both 3C 390.3 and 3C 120, indicates that a time-averaged spectral analysis might not be the most appropriate tool for the diagnostic of physical conditions in the inner regions of 3C 390.3 and 3C 120. However, the limited signal-to-noise ratio of HEXTE data allows only a time-averaged spectral analysis. Moreover, even if the spectral index of the “primary” power-law spectrum does vary with luminosity, the spectral features resulting from the reprocessing of the primary X-rays in the accretion disk should not be significantly affected by these spectral-index fluctuations, especially since the range of variation turns out to be small (see §4.2, below). The primary cause of fluctuations in the reprocessing features is the variation of the primary power-law intensity, which itself spans a range of approximately a factor of 2. Under these conditions, we expect that the spectrum of reprocessed X-rays varies mainly in intensity and not in any other way (see, for example, Ballantyne & Ross 2002). Thus we use the time-averaged spectrum primarily to evaluate reprocessing models and not models for the primary continuum. Therefore, we first performed a time-averaged analysis using the PCA and HEXTE data together, in the attempt to constrain the Compton “reflection” component. In a second pass we analyzed time-resolved PCA spectra of 3C 390.3 to study the evolution of the spectral index and possible variations of the Fe $K\alpha$ line flux over the course of the large, systematic decline displayed during the first half of the monitoring period.

The spectral analysis of PCA and HEXTE data was performed using the `XSPEC v.11` software package (Arnaud 1996). We used PCA response matrices and effective area curves created specifically for the individual observations by the program `pcarsp`, taking into account the evolution of the detector properties. To fit the HEXTE spectra we used response matrices and effective area curves created on 1997 March 20. The PCA spectra (with the appropriate response matrices) were first extracted selecting several short time intervals to take into account the different number of PCUs at work and any possible change in calibration; subsequently, all the spectra were combined with `addspec`. All the spectra were rebinned so that each bin contained enough counts for the χ^2 statistic to be valid. Fits were performed in the energy ranges 4–20 keV (PCA), 20–50 keV (HEXTE), where the signal-to-noise ratio is the highest. Joint fits to PCA+HEXTE spectra were carried out allowing the normalization factors for each instrument to be a free parameter.

4.1. Time-Averaged Spectra

We first fitted the combined PCA+HEXTE spectra of 3C 390.3 and 3C 120 with a simple power-law with Galactic absorption. The very poor fits ($\chi^2 = 420.6/49 \text{ dof}$ and $\chi^2 = 885.8/67 \text{ dof}$, for 3C 390.3 and 3C 120 respectively), clearly indicate the need for a different continuum model or, at least, of an additional component. In fact, adding a Gaussian line improved the spectral fits significantly. This is clearly evident in Figure 9, where we plot the residuals to the PCA+HEXTE spectrum of 3C 120 for a simple power-law model (top panel), a power-law plus a Gaussian component at 6.4 keV (middle panel), a broken power-law plus a Gaussian line at 6.4 keV (bottom panel). Similar results are obtained for 3C 390.3.

The rather weak reflection component usually found in BLRGs can be interpreted either in terms of a truncation of the innermost parts of the optically-thick accretion disk (thought to be the main “reflector”) or, as recently suggested by Ballantyne et al. (2002), as a result of reprocessing in an *ionized* accretion disk. For this reason, as models of the continuum, apart from a single power-law and a broken power-law, we tried a power-law plus its Compton reflection, implemented in XSPEC as `pexrav` (Magdziarz & Zdziarski 1995) and the constant-density ionized-disk reflection model (Ross & Fabian 1993, Ballantyne et al. 2001) available as a table model in XSPEC v11.2. Figure 10 shows the residuals of the PCA+HEXTE spectrum of 3C 390.3 for the `pexrav` model (top panel) and for the constant-density ionized-disk reflection model (bottom panel), with an additional Gaussian line at 6.4 keV. In the latter model, the accretion disk is approximated as a slab of gas with constant density ($n_{\text{H}} = 10^{15} \text{ cm}^{-3}$) and solar abundances, which is illuminated by X-rays with a flux F_{x} (extending from 1 eV to 100 keV) and a power-law spectrum of photon index Γ . The reflected spectrum is scaled according to the solid angle of the absorber ($R \equiv \Omega/2\pi$), and then added to the incident spectrum to give the final observed spectrum. The structure of the reflected spectrum is determined by the ionization parameter $\xi = 4\pi F_{\text{x}}/n_{\text{H}}$. This model predicts the Fe $K\alpha$ emission line and the spectral features at low energy (emission lines and recombination continuum). An additional Gaussian line at 6.4 keV (in the source rest frame) is needed by all the continuum models to account for the strong excess around 6.4 keV. The results of fitting the above models are summarized in Tables 4 and 5.

For both sources the best-fit is obtained using broken power-law models: $\Delta\chi^2$ ranges between 11 (for 3C 390.3) and 60 (for 3C 120), which is significant at more than 99% confidence for two additional free parameters, with respect to the fit with a single power-law. However, since a broken power-law model is an *ad hoc* phenomenological model, it is difficult to draw information on the physical conditions of the accretion flow from spectral fits with this model. More useful information can be derived by comparing the spectral fits

of models assuming reflection from a neutral and from an ionized accretion disk, respectively. The first important result is that the ionized disk reflection model gives a better description of the time-averaged spectra of 3C 390.3 and 3C 120 (fits with `pexrav`, which has an additional free parameter with respect to the ionized disk model, result in a significant increase of the total χ^2). However, for both sources the inferred ionization parameter is not high, $\xi \simeq 300$, which is nearly a factor 10 lower than the value derived for 3C 120 by Ballantyne et al. (2002) using a 50 ks observation from ASCA, with the reflection fraction fixed at 1. We tried to fit the ionized disk model with the reflection fraction fixed at 1 to the *RXTE* data of 3C 390.3 and 3C 120, but the resulting χ^2 are not acceptable. The reflected fraction (i.e., $\Omega/2\pi$) is negligible according to both the neutral and the ionized disk models (consistent with zero for 3C 390.3). To assess whether the results from the time-averaged spectral analysis are reliable (in view of the spectral variability shown by the X-ray color analysis; see §3.3), we have fitted nine time-resolved PCA spectra plus the average HEXTE spectrum of 3C 390.3 with the neutral and ionized-disk models. The main results are the following: 1) the spectra are better fitted by an ionized-disk in six cases out of nine; 2) the spectral parameters, with the exception of the folding energy for `pexrav` do not vary significantly and are basically consistent with the time-averaged values: the reflection is low for both models and the parameter ξ in the ionized-disk model is always small, but not consistent with zero.

While the reflection component is weak, a strong iron line is required in all the spectral fits (if the spectral model used to fit the continuum is not the ionized-disk). The Fe $K\alpha$ line was modeled as a Gaussian of energy dispersion σ , and intensity $I_{\text{Fe}K\alpha}$. Due to the low spectral resolution of the PCA, we did not use more sophisticated models for the line profile. Since HEXTE spectra do not extend below 20 keV, for both objects we used only the PCA data, for which a power-law + Gaussian line give acceptable fits of the spectra. Both 3C 390.3 and 3C 120 have relatively broad ($\sigma \simeq 0.4$ keV), relatively strong ($I_{\text{Fe}K\alpha} = 5 - 10 \times 10^{-5}$ photons $\text{s}^{-1} \text{cm}^{-2}$) iron lines, with centroids consistent with the value of “cold” Fe $K\alpha$. On the other hand, using the ionized-disk model to fit the continuum, the parameters of the additional Gaussian line have much lower values: $\sigma \simeq 0.2$ keV, $I_{\text{Fe}K\alpha} = 3 \times 10^{-5}$ photons $\text{s}^{-1} \text{cm}^{-2}$. The reason for this discrepancy is that the ionized-disk model already includes the Fe $K\alpha$ emission line; as a consequence, part of the excess around 6.4 keV is already accounted for by the reprocessing model. A natural question that can be raised at this point is: why an additional Gaussian component is necessary also for the ionized-disk model? There are two possible explanations: 1) if the line originates from an inner region close to the black hole, relativistic effects become important, but they are not taken into account by the constant-density ionized-disk model available in `XSPEC`; 2) the iron line emission is complex, possibly made of two main components: a broad component originating from the inner part of the accretion disk, and a second narrow one probably

associated with a region distant from the central source. Such a narrow line component has been detected in several Seyfert 1 galaxies with *Chandra* (e.g., Yaqoob et al. 2001, Kaspi et al 2001) and *XMM-Newton* (e.g., Pounds et al. 2001, Reeves et al. 2001). It also is worth noting that De Rosa et al. (2002) found that the BeppoSAX spectrum of the Seyfert 1 galaxy NGC 7469 was best fitted with the ionized-disk model and a second narrow line component, in addition to that produced in the disk, was also required to fit the iron line profile. Spectral parameters of the Fe K α line in 3C 390.3 and 3C 120 are reported in Table 5 and contour plots of the energy dispersion σ and the Fe K α photon flux are shown in Figure 11, indicating that in both sources the Fe K α is resolved at more than 99% confidence level.

4.2. Time-Resolved Spectra

Since the data consist of short snapshots spanning a long temporal baseline, they are well suited for monitoring the spectral variability of the sources and represent the ideal tool for the diagnostic of the changing physical conditions of the matter around the supermassive black hole. A test of scenarios for the geometry of the accretion flow is afforded by the correlated or delayed variability of the Fe K α line flux with the X-ray continuum flux (in effect, X-ray reverberation mapping), as different time delays are expected depending on the location of the cold reprocessor with respect to the X-ray source. If the Fe K α line originates from the outer regions of an ADAF, the time delay between the line and the continuum should be of the order of a few days or larger. Shorter delays (≤ 1 day) are expected if the line originates from the inner parts of a disk extending further in, as in Seyferts. Finally, if the line comes from the molecular torus, the delays will be of the order of several months or longer.

In an attempt to constrain the location of the gas responsible for the Fe K α emission line in 3C 390.3, we performed an X-ray “reverberation mapping” study. This consists in the study of possible delayed variations of the Fe K α line flux with the 2–10 keV continuum. Of our two sources, 3C 390.3 is the most suitable for performing a study of the Fe K α line flux variability because of the systematic trend of variability observed (Figure 1). We divided the light curve of Figure 1 into nine intervals, with exposures ranging between 10 ks and 25 ks, which represent a trade-off between the necessity to isolate intervals with different but well defined average count rates and the need to reach a signal-to-noise ratio high enough for a meaningful spectral analysis. The dates, exposure times and mean fluxes in the nine selected intervals are listed in Table 6.

We fitted the 4–20 keV spectra with a model consisting of a power-law, absorbed by the Galactic absorbing column, plus a Gaussian Fe K α line with a rest energy fixed at 6.4

keV. We did not use the constant-density ionized model to fit the continuum because, as explained above, although it already includes the Fe K α line, it does not allow us to measure line parameters. The results of the fits are summarized in Table 7. Due to the combination of a short exposure and a low count rate, the spectral data of the ninth interval have low signal-to-noise ratio and therefore the spectral parameters inferred from the fit are characterized by large errors. For this reason we will not use these values in the following analysis.

The top panel of Figure 12 shows the light curves of the Fe K α line flux while the bottom panels shows the 2–10 keV flux for comparison. Because of the large error bars, we can only speculate about the implications of this diagram. Neglecting the errors, one might argue that the maximum of the Fe K α line flux light curve appears to be shifted by ~ 20 days compared to the 2–10 keV flux maximum, however the significance of the Fe K α line flux variability is statistically questionable. A χ^2 test shows that the Fe K α light curve is consistent with being constant ($\chi_r^2 = 0.6$ for 8 d.o.f.; $P_{\chi^2} \simeq 80\%$), which discouraged us from attempting more sophisticated tests, such as cross-correlation analysis.

Even the PCA sensitivity is not sufficient to obtain reliable results from the time-resolved X-ray spectroscopy. Nevertheless, valuable information can be obtained by plotting spectral parameters against the 2–10 keV flux. Figure 13 shows the plots of the photon index Γ (top panel) and Fe K α line flux (bottom panel) versus the 2–10 keV flux (10^{-11} erg s $^{-1}$ cm $^{-2}$). The main results are the following: the photon index increases with the 2–10 keV flux, with some indications of a flattening at higher fluxes. The Fe K α line flux also increases as the 2–10 keV flux increases, but only for a limited range of fluxes; at larger continuum flux values the Fe K α line flux is roughly constant.

Probably only *XMM-Newton* with its superior sensitivity and the possibility of long continuous observations will be able to achieve significant results in this kind of analysis.

5. Summary and Discussion

We have presented a temporal and spectral analysis of two long (~ 60 days) *RXTE* observations of the BLRGs 3C 390.3 and 3C 120 performed in May-July 1996 and January-March 1997, respectively. The first important result of the timing analysis is that the two sources behave differently. This does not necessarily imply that the two BLRGs are intrinsically different, only that they have been caught during different facets of their temporal behavior. The qualitative difference inferred by the visual inspection of the light curves is quantified by the structure function analysis, which shows that 3C 390.3 has a characteristic timescale of ~ 20 days (i.e., its decaying time), while no typical timescale is found for 3C 120.

Also the flux variability, quantified in terms of the fractional variability parameter F_{var} , is different: 3C 390.3 is significantly more variable than 3C 120, despite its jet inclination angle inferred from radio observations ($19^\circ \leq i \leq 33^\circ$) is larger than that of 3C 120 ($1^\circ \leq i \leq 14^\circ$). A straightforward interpretation of this first result is that the X-ray variability we observe is not related to (or, at least, not dominated by) the relativistic jet associated with the central engine. More specifically, in the case of 3C 390.3, significant variations occur on a time scale of order a month, which is longer than the typical variability time scale of blazars (e.g., Kataoka, Takahashi, & Wagner 2001). In the case of 3C 120, there are clear variations from day to day, but their amplitude is of order 10%, for which we offer the following plausible interpretation. We hypothesize that the observed X-ray flux is a combination of variable emission from the relativistic jet and steady emission from a source associated with the inner accretion disk. If we take the jet emission to be variable by a factor of 2 about its mean level, then the observed variations at a level of 10% imply that the contribution of the jet emission to the total observed flux is only 5%. The limited contribution of the jet X-ray emission is also confirmed by the X-ray spectrum, which shows a prominent Fe $K\alpha$ line.

As a consequence, the X-ray observations of these objects would probe the physical conditions of the central engine with very little contamination from the radiation originating from the base of the jet. Alternatively, the difference in flux variability pattern between the two sources can be explained assuming that there are at least two different processes simultaneously at work in 3C 390.3: one (not related to the jet) causing the smooth secular decay observed throughout the X-ray monitoring and another (possibly connected to the jet) giving rise to the small-amplitude flares superimposed to the long-term variation in the 3C 390.3 light curve (and to the erratic flux variation displayed by the 3C 120 light curve). The idea of a contribution from two different physical processes to the variability of 3C 390.3 is supported by the different variability behavior in the first (smooth flux decline) and second part (flux roughly constant) of the light curve, as seen in the color-color plot (see Figure 8).

Other important findings from the temporal analysis are obtained by applying the fractional variability analysis to energy-selected light curves and to time-selected intervals of the total light curve. From the former analysis we found that the fractional variability amplitude is strongly anticorrelated with the energy band in both sources. This behavior is qualitatively in agreement with the scenario where X-rays are produced by Compton up-scattering in a hot corona located above the accretion disk, which emits the primary soft flux (e.g., Haardt & Maraschi 1991). In this scenario the hard photons are produced by a larger number of scatterings and therefore their variability is washed out. The result of the fractional variability analysis of energy-selected light curves is also important from another point of view, since it reinforces the claim that the X-rays observed in 3C 390.3 and 3C 120 originate from the central region and not from the base of a putative X-ray jet. In fact,

a similar analysis carried out on blazars (e.g., Fossati et al. 2000, Chapman et al. 2002), whose emission is thought to be dominated by non-thermal radiation from relativistic jets seen at small angles to the line of sight, shows an opposite trend, with the flux variability increasing with the energy, and can be simply explained in terms of shorter cooling time for more energetic electrons.

From the time-resolved fractional variability analysis, 3C 390.3 does not show any significant correlation, while the fractional variability of 3C 120 is weakly anticorrelated with the count rate. While the existence of an anticorrelation between source luminosity and variability amplitude among radio-quiet AGN is well known (e.g., Lawrence & Papadakis 1993, Nandra et al. 1997, Leighly 1999), to the best of our knowledge 3C 120 represent the first example where this inverse correlation is found for individual objects. This kind of analysis, along with the use of other techniques not generally applied to AGN light curves (i.e., Gliozzi et al. 2002) can potentially provide useful information to advance our understanding of the X-ray variability in AGN. However, the lack of long X-ray light curves of AGNs with high signal-to-noise ratio prohibits us from carrying out a systematic analysis on a large sample. It is worth noting that a similar study was recently carried out by Turner et al. (2001) on a 35 day ASCA observation of the bright Narrow-Line Seyfert 1 galaxy Akn 564, and no clear correlation was found between the fractional variability and X-ray flux for this source. On the other hand, in jet dominated AGN F_{var} is positively correlated with the count rate (e.g., Zhang et al. 1999, Chapman et al. 2002).

Another remarkable result is the pronounced spectral variability, as shown by the large-amplitude variations of the X-ray colors, and the anti-correlation between the color and the local mean count rate. A similar trend with the spectrum becoming steeper as the flux increases was already noticed in sub-sample of hard X-ray-selected AGN (Grandi et al. 1993), and recently confirmed for Seyfert galaxies by Markowitz & Edelson (2001) and Papadakis et al. (2002). This trend can be naturally explained in terms of a variation of the spectral slope, which is predicted by thermal Comptonization models. However, not all AGNs show the same spectral behavior (e.g., Grandi et al. 1993) with some objects showing no energy dependence of their variability (e.g., Vaughan 2001) or even a hardening of the spectrum as the source gets brighter (e.g., Gliozzi et al. 2001).

The main results derived from the time-averaged spectral analysis are (a) a strong and resolved Fe $K\alpha$ line in 3C 390.3 and 3C 120, and (b) a reflection component that is quite weak (unnecessary in the case of 3C 390.3). The spectral parameters of 3C 390.3 and 3C 120 are roughly consistent with previous studies (e.g., Woźniak et al. 1998, Grandi et al. 1999, Eracleous et al. 2000, Zdziarski & Grandi 2001), with the Compton reflection component weaker and the Fe $K\alpha$ line stronger than the values reported in literature. A common

explanation for the usually weak reflection component found in radio-loud AGNs is that the solid angle subtended by the largely neutral reprocessor is smaller. Since the reprocessor is widely thought to be a standard optically-thick accretion disk, this has led to speculation that the standard disk might be truncated with an optically-thin flow in the inner region. An alternative interpretation, recently proposed by Ballantyne et al. (2002), is that the accretion disk is ionized. In order to test such hypothesis we have fitted the time-averaged spectra of 3C 390.3 and 3C 120 with the constant-density ionized-disk model of Ross & Fabian (1993, Ballantyne et al. 2001) and found a statistically significant improvement in the spectral fits with respect to those obtained with the `pexrav` model. The time-averaged spectral analysis thus favors the presence of an ionized disk, but with a moderate ionization parameter ($\xi \simeq 300$). Following Ballantyne et al. (2002), we also tried to fit the *RXTE* spectra of 3C 390.3 and 3C 120 keeping the reflection fraction fixed to 1; however, the resulting χ^2 were not acceptable in either cases.

The monitoring strategy consisting of short, closely spaced, snapshots on a long temporal baseline, along with the rather smooth changes in the X-ray flux shown by 3C 390.3, allowed us to search for correlations or delays in the variability pattern of the continuum and the Fe $K\alpha$ line. The detection of correlated or delayed line and continuum variability would be a very powerful diagnostic of the location of the line emitting region. Unfortunately, though, neither our results nor those of other studies of BLRGs have shown such an effect. In the case of our study, the S/N of the Fe $K\alpha$ line in time resolved spectra is not high enough to show the line variability expected from the observed continuum variations. Other authors (e.g., Wòzniak et al. 1998 for 3C 390.3, Grandi et al. 2001 for 3C 382) have claimed that the line intensity in BLRGs does not track the variations of the continuum, but their conclusions are based on very sparsely sampled light curves (6 and 3 observations, respectively, spanning a decade) taken with different instruments. Moreover, the values of the line flux might be affected by the different spectral models used for the fit of the continuum and by the different calibrations of the instruments. Thus, the above conclusions can be stated more precisely by saying that the light-crossing time of the Fe $K\alpha$ -emitting region is longer than the duration of a typical observation, which is of the order of a day. This is not a very strong constraint if one notes that the light-crossing time of the inner accretion disk ($r \sim 10GM/c^2$) of $10^9 M_\odot$ black hole is approximately 0.6 days.

Interesting results are found by plotting spectral parameters versus the 2–10 keV flux. First, we found that the spectral variability (already inferred by the color analysis) is due to intrinsic changes in the photon index, which gets steeper as the flux increases. A similar spectral behavior was already noticed in 3C 120 by Halpern (1985), who interpreted it in terms of beamed synchrotron emission from a relativistic jet. But in view of our results and our discussion above, emission from the jet makes a very small contribution to the

observed flux. Therefore, we prefer a scenario in which such spectral variability can be simply explained with the standard scenario of thermal Comptonization from a hot corona, widely accepted for radio-quiet AGN. Even more interesting is the Fe $K\alpha$ line flux, which shows an initial increase as the 2–10 keV flux increases and a stationary low level at higher values of the X-ray continuum. However, the large errors associated with the time-resolved spectral analysis suggest that such results should be regarded with caution; yet these results should serve as a motivation to perform more sensitive X-ray monitoring observations with new generation X-ray satellites as *XMM-Newton*.

6. Conclusion

A detailed comparison of the temporal and spectral variability properties of BLRGs with those of jet-dominated and of radio-quiet AGN leads to two important results: (a) the jet contribution to the X-ray flux in BLRGs is negligible, and (b) BLRGs qualitatively behave according to the standard scenario of thermal Comptonization, widely accepted for radio-quiet AGN. However, the observational data available at the moment do not give a conclusive answer to the question of the structure of the inner accretion disks of BLRGs in particular and radio-loud AGNs in general. On one hand, the X-ray variability properties of BLRGs seem to be similar to those of Seyfert galaxies suggesting a common emission process. Moreover, model fits to the *ASCA* X-ray spectrum of 3C 120 (Ballantyne et al. 2002) favor a highly ionized accretion disk. On the other hand, the high-S/N *RXTE* spectra presented here are best fitted with models in which the disk ionization is modest. In addition, *ASCA* observations of BLRGs such as 3C 390.3 and 3C 445 (e.g., Eracleous, Halpern, & Livio 1995; Sambruna et al. 1998) suggest that the Fe $K\alpha$ lines of these objects come from low-ionization gas. It is unfortunate that the easily measurable quantities, such as the Fe $K\alpha$ EW and the strength of the Compton reflection component, are ambiguous indicators of the ionization state of the disk.

To further address the above issues and to test the hypothesis of the presence of an ionized accretion disk, a crucial step forward may be achieved by future X-ray monitoring campaigns and/or high-S/N spectra with *XMM-Newton*. In fact the possibility of long uninterrupted observations combined with the superior sensitivity of EPIC should allow one to perform an accurate time-resolved analysis. Moreover, the broad-band X-ray spectrum extending down to 0.2 keV would be important to assess the presence of a moderately ionized disk, which is supposed to show strong emission lines (C,N,O) in the soft X-ray range.

MG and RMS acknowledge financial support by NASA LTSA grant NAG5-10708. Sup-

port from NASA grant NAG5-10243 is also acknowledged. ME acknowledges support from NASA grants NAG5-7733, NAG5-8369, and NAG5-9982. During the early stages of this project, ME was based at the University of California, Berkeley and was supported by Hubble Fellowship grant HF-01068.01-94A, awarded by the Space Telescope Science Institute.

REFERENCES

- Arnaud, K. 1996, in ASP Conf. Ser. 101, *Astronomical Data Analysis Software and Systems V*, ed. G. Jacoby & J. Barnes (San Francisco: ASP), 17
- Ballantyne, D.R., Ross, R.R., & Fabian, A.C. 2001, *MNRAS*, 327, 10
- Ballantyne, D.R., Ross, R.R., & Fabian, A.C. 2002, *MNRAS* in press, (astro-ph/0201403)
- Ballantyne, D.R. & Ross, R.R. 2002, *MNRAS* in press, (astro-ph/0201420)
- Chapman, E., Sambruna, R., Gliozzi, M., et al. 2002, in prep
- De Rosa, A., Fabian, A.C. & Piro, L. 2002, *MNRAS* in press (astro-ph/0205347)
- Edelson, R., Turner, T.J., Pounds, K., et al. 2002, *ApJ*, 568, 610
- Eracleous, M., & Halpern, J.P. 1998, *ApJ* 505, 577
- Eracleous, M., Halpern, J. P. & Livio, M. 1996, *ApJ*, 459, 89
- Eracleous, M., Sambruna, R., & Mushotzky, R.F. 2000, *ApJ*, 537, 654
- Fossati, G., Celotti, A., Chiaberge, M., et al., 2000, *ApJ*, 541, 153
- Grandi, P., Tagliaferri, G., Giommi, P., Barr, P., & Palumbo, G. 1992, *ApJS*, 82, 93
- Grandi, P., Sambruna, R., Maraschi, L., et al. 1997, *ApJ*, 487, 636
- Grandi, P., Guainazzi, M., Haardt, F., et al., 1999 *A&A* 343, 33
- Grandi, P., Urry, C. M., & Maraschi, L. 2002, *New Astr. Rev.* 46, 221
- Grandi, P., Urry, C. M., Maraschi, L., & Matt, G. 2001, *ApJ* 556, 35
- Gliozzi, M., Brinkmann, W., O’Brien, P.T., et al., 2001, *A&A*, 365, L128
- Gliozzi, M., Brinkmann, W., R ath, C., et al. 2002, *A&A* in press (astro-ph/0206190)
- Haardt, F., & Maraschi, L., 1991, *ApJ*, 380, L51
- Halpern, J. 1985, *ApJ*, 290, 130
- Hasenkopf, C.A., Sambruna, R.M., & Eracleous, M. 2002, *ApJ*, 575, in press, (astro-ph/0204257)
- Hasinger, G. & van der Klis, M. 1989, *A&A*, 225, 79
- Hughes, P.A., Aller, H.D., Aller, M.F., 1992, *ApJ*, 396, 469
- Jahoda, K., Swank, J., Giles, A.B., et al. 1996, *Proc.SPIE*, 2808, 59
- Kaspi, S., Brandt, W.N., Netzer, H., et al. 2001, *ApJ*, 554, 216
- Kataoka, J., Takahashi, T., Wagner, S.J., et al., 2001, *ApJ*, 560, 659

- Lawrence, A., & Papadakis, I.E. 1993, ApJ, 414, L85
- Leighly, K.M., & O’Brien, P. 1997, ApJ, 481, L15
- Leighly, K.M. 1999, ApJS 125, 297
- Magdziarz, P., & Zdziarski, A.A. 1995, MNRAS, 273, 837
- Markowitz, A., & Edelson, R. 2001, ApJ, 547, 684
- Nandra, K., George, I., Mushotzky, R.F., Turner, T.J., & Yaqoob, T. 1997, ApJ, 476, 70
- Narayan, R., Mahadevan, R., & Quataert, E. 1998, in “Theory of Black Hole Accretion Disks,” eds. M. A. Abramowicz, G. Bjornsson, & J. E. Pringle (Cambridge: Cambridge University Press), 148
- Papadakis, I.E., Petrucci, P.O., Maraschi, L., et al., 2002, ApJ, 573, 92
- Pounds, K., Reeves, J., O’Brien, P., et al., 2001, ApJ, 559, 181
- Reeves, J., Turner, M., Pounds, K., et al., 2001, A&A, 365, L134
- Rodriguez-Pascual, P.M., Alloin, D., Clavel, J., et al. 1997, ApJS, 110, 9
- Ross, R.R. & Fabian, A.C., 1993, MNRAS, 261, 74
- Rotschild, R.E., Blanco, P.R., Gruber, D.E., et al. 1998, ApJ, 496, 538
- Sambruna, R.M., Eracleous, M., & Mushotzky, R.F. 1999, ApJ, 526, 60
- Sambruna, R.M. & Eracleous, M. 2002, AIP Conference Proceedings, Vol. 599, 355, ed. N.E. White, G. Malaguti, G.G.C. Palumbo
- Sambruna, R. M., George, I. M., Mushotzky, R. F., Nandra, K., Turner, T. J. 1998, ApJ, 495, 749
- Simonetti, J.H., Cordes, M.J., Heeschen, D.S., 1985, ApJ, 296, 46
- Turner, T.J., George, I.M., Nandra, K., & Turcan, D. 1999, ApJ, 524, 667
- Turner, T.J., Romano, P., George, I.M., et al. 2001, ApJ, 561, 131
- van der Klis, M. 1995, in X-Ray Binaries, eds. W. H. G. Lewin, J. van Paradijs, and E. P. J. van den Heuvel (Cambridge: Cambridge University press), 252
- Vaughan, S., 2001, in Proceedings of the JHU Workshop on Accretion Disks, ed. T. Yaqoob
- Woźniak, P.R., Zdziarski, A.A., Smith, D., Madejski, G.M., & Johnson, W.N. 1998, MNRAS, 299, 449
- Yaqoob, T., George, I.M., Nandra, K., et al. 2001, ApJ, 546, 759
- Zdziarski, A.A., & Grandi, P. 2001, ApJ, 551, 186

Zhang, Y.H., Celotti, A., Treves, A., et al. 1999, ApJ, 527, 719

.8.8

This preprint was prepared with the AAS L^AT_EX macros v5.0.

Table 1. Targets: Basic Properties and Observation Log

Object	z	i^a ($^\circ$)	$N_{\text{H,Gal}}$ (cm^{-2})	Start Time (UT) (yy/mm/dd hh:mm)	End Time (UT) (yy/mm/dd hh:mm)
3C 390.3	0.056	$19 \leq i \leq 33$	3.74×10^{20}	1996/05/17 14:14	1996/07/12 21:43
3C 120	0.033	$1 \leq i \leq 14$	1.20×10^{21}	1997/01/10 11:43	1997/03/08 05:14

^a The inclination angle of the radio jet (Eracleous & Halpern 1998)

Table 2. Observation Details: Total Exposure Times and Count Rates

Object	PCA (2–20 keV)		HEXTE (20–50 keV)	
	Exposure (ks)	Count Rate (s^{-1})	Exposure (ks)	Count Rate (s^{-1})
3C 390.3	132.14	10.53 ± 0.02	42.72	0.19 ± 0.02
3C 120	126.18	18.53 ± 0.02	40.23	0.57 ± 0.05

Table 3. Fractional Variability of 3C 390.3 and 3C 120

Object	Band (keV)	$\langle rate \rangle$ (s^{-1} PCU $^{-1}$)	F_{var} (5760 s)	χ^2_{red}, P_{χ^2}	r, P_c
3C 390.3	2–5	0.43	$(30.8 \pm 1.9) \times 10^{-2}$	2.6, 7%	-0.999, 2%
	5–7	0.74	$(28.3 \pm 1.6) \times 10^{-2}$		
	7–11	1.06	$(25.5 \pm 1.5) \times 10^{-2}$		
3C 120	2–5	1.09	$(8.9 \pm 0.6) \times 10^{-2}$	6.4, $\ll 1\%$	-0.975, 10%
	5–7	1.75	$(8.1 \pm 0.5) \times 10^{-2}$		
	7–11	2.35	$(6.4 \pm 0.4) \times 10^{-2}$		

Table 4. Results of Model Fits to Time-Averaged Spectra

Model	Parameters	3C 390.3	3C 120
Simple Power-Law	Photon index, Γ	1.70 ± 0.01	1.84 ± 0.01
	Reduced χ^2 /d.o.f	1.06/47	1.80/61
Broken Power-Law	Low-energy photon index, Γ_1	1.70 ± 0.01	1.81 ± 0.01
	Break energy (keV)	30^{+80}_{-10}	9 ± 1
	High-energy photon index, Γ_2	1.40 ± 0.05	$1.69^{+0.03}_{-0.04}$
	Reduced χ^2 /d.o.f	0.86/45	0.83/59
Power-Law Plus	Photon index, Γ	1.72 ± 0.02	$1.83^{+0.05}_{-0.06}$
Neutral Disk Reflection	Folding energy ^a (keV)	14,200 (140)	130 (50)
	Reflector solid angle, $\Omega/2\pi$	0.1 ± 0.1	0.4 ± 0.2
	Inclination angle, i (deg) ^b	33	11
	Reduced χ^2 /d.o.f	1.05/44	0.91/58
Power-Law Plus	Photon index, Γ	1.71 ± 0.01	1.84 ± 0.01
Ionized Disk Reflection	Log(ionization parameter), $\log \xi$	$2.5^{+0.2}_{-0.3}$	$2.4^{+0.1}_{-0.6}$
	Reflector solid angle, $\Omega/2\pi$	$0.2^{+0.1}_{-0.2}$	$0.3^{+0.1}_{-0.2}$
	Reduced χ^2 /d.o.f	0.94/45	0.83/59

^aBest fitting values and 90% confidence lower limits obtained with the **steppar** procedure.

^bBest fitting value.

Table 5. Parameters of Gaussian Emission-Line Models

Parameter	3C 390.3		3C 120	
	Power-law	Ionized-disk	Power-law	Ionized-disk
Rest energy (keV)	$6.42^{+0.09}_{-0.07}$	$6.29^{+0.16}_{-0.31}$	$6.39^{+0.04}_{-0.05}$	$6.21^{+0.19}_{-0.23}$
Rest energy dispersion, σ (keV)	$0.43^{+0.14}_{-0.09}$	$0.26^{+0.17}_{-0.26}$	$0.37^{+0.06}_{-0.04}$	$0.16^{+0.16}_{-0.16}$
Line flux ($10^{-5} \text{ s}^{-1} \text{ cm}^{-2}$)	$5.2^{+0.9}_{-0.8}$	$2.6^{+2.3}_{-1.1}$	$9.9^{+0.6}_{-0.6}$	$3.2^{+4.3}_{-1.1}$
Equivalent width (eV)	170 ± 30	82^{+73}_{-33}	150^{+8}_{-10}	45^{+58}_{-16}

Table 6. Time Intervals Used for Time-Resolved Spectral Analysis

Start Time (UT) (yy/mm/dd hh:mm)	End Time(UT) (yy/mm/dd hh:mm)	Exposure (ks)	2–10 keV Flux (10^{-11} erg cm $^{-2}$ s $^{-1}$)
96/05/17 14:14	96/05/21 13:33	11.84	3.70
96/05/22 20:54	96/05/26 15:08	10.30	3.12
96/05/27 16:05	96/05/28 21:47	12.33	3.22
96/06/01 15:50	96/06/05 10:12	13.22	2.90
96/06/06 19:09	96/06/10 14:48	13.25	2.20
96/06/11 12:35	96/06/15 03:33	14.26	1.98
96/06/18 22:13	96/06/27 00:21	27.28	1.74
96/06/27 19:55	96/07/02 21:02	21.02	1.84
96/07/07 13:43	96/07/12 22:33	8.64	2.25

^aCalculated assuming a power law plus Gaussian line model.

Table 7. Time-resolved spectral parameters

Photon Index	Energy Dispersion (keV)	Line Flux (10^{-5} cm $^{-2}$ s $^{-1}$)	Equivalent Width (eV)
1.79 ± 0.04	$0.3^{+0.6}_{-0.3}$	7^{+4}_{-3}	140^{+90}_{-70}
1.73 ± 0.03	$0.3^{+0.6}_{-0.3}$	5^{+3}_{-2}	130^{+80}_{-60}
1.75 ± 0.03	$1.5^{+1.1}_{-1.0}$	6^{+3}_{-2}	150^{+70}_{-50}
1.71 ± 0.03	$0.2^{+0.4}_{-0.2}$	6 ± 2	150^{+70}_{-40}
1.71 ± 0.04	0.8 ± 0.3	9 ± 3	340^{+120}_{-110}
$1.62^{+0.04}_{-0.05}$	0.7 ± 0.4	7^{+4}_{-3}	270^{+150}_{-110}
$1.60^{+0.03}_{-0.04}$	$0.2^{+0.3}_{-0.2}$	4^{+2}_{-1}	180^{+70}_{-50}
$1.69_{\pm 0.04}$	$0.4^{+0.3}_{-0.4}$	5^{+3}_{-1}	200^{+110}_{-60}
$1.69^{+0.11}_{-0.05}$	$1.4^{+2.1}_{-1.4}$	7^{+28}_{-6}	200^{+900}_{-200}

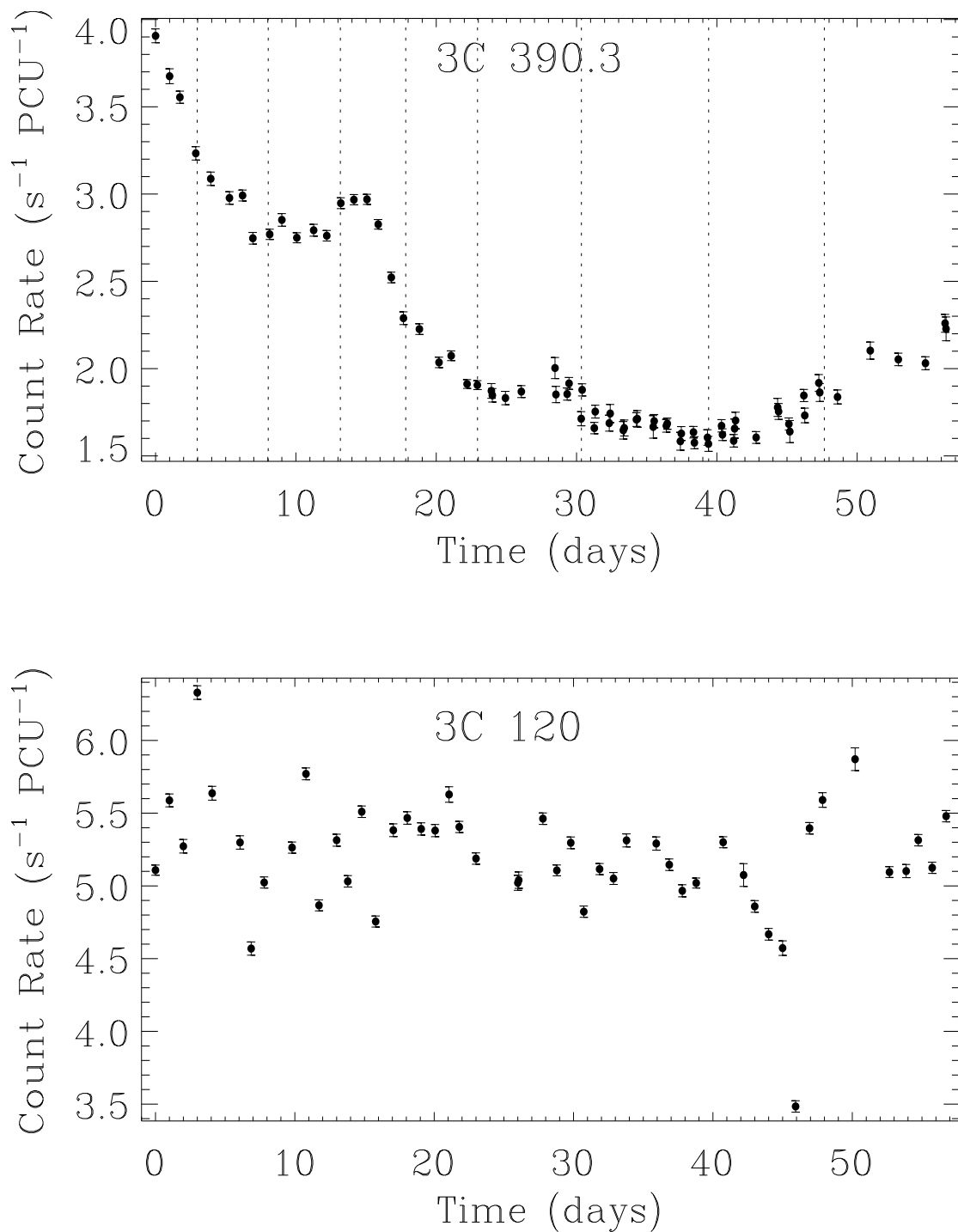


Fig. 1.— X-ray light curves of 3C 390.3 (top panel) and 3C 120 (bottom panel) from *RXTE* PCA observations in the 2–11 keV band. Time bins are 5760 s (\sim one *RXTE* orbit). For the sake of clarity, only data bins which were at least 10% full are plotted here, although all the data were used in the analysis. The dotted lines in the top panel indicate the intervals used for the time-resolved spectral analysis.

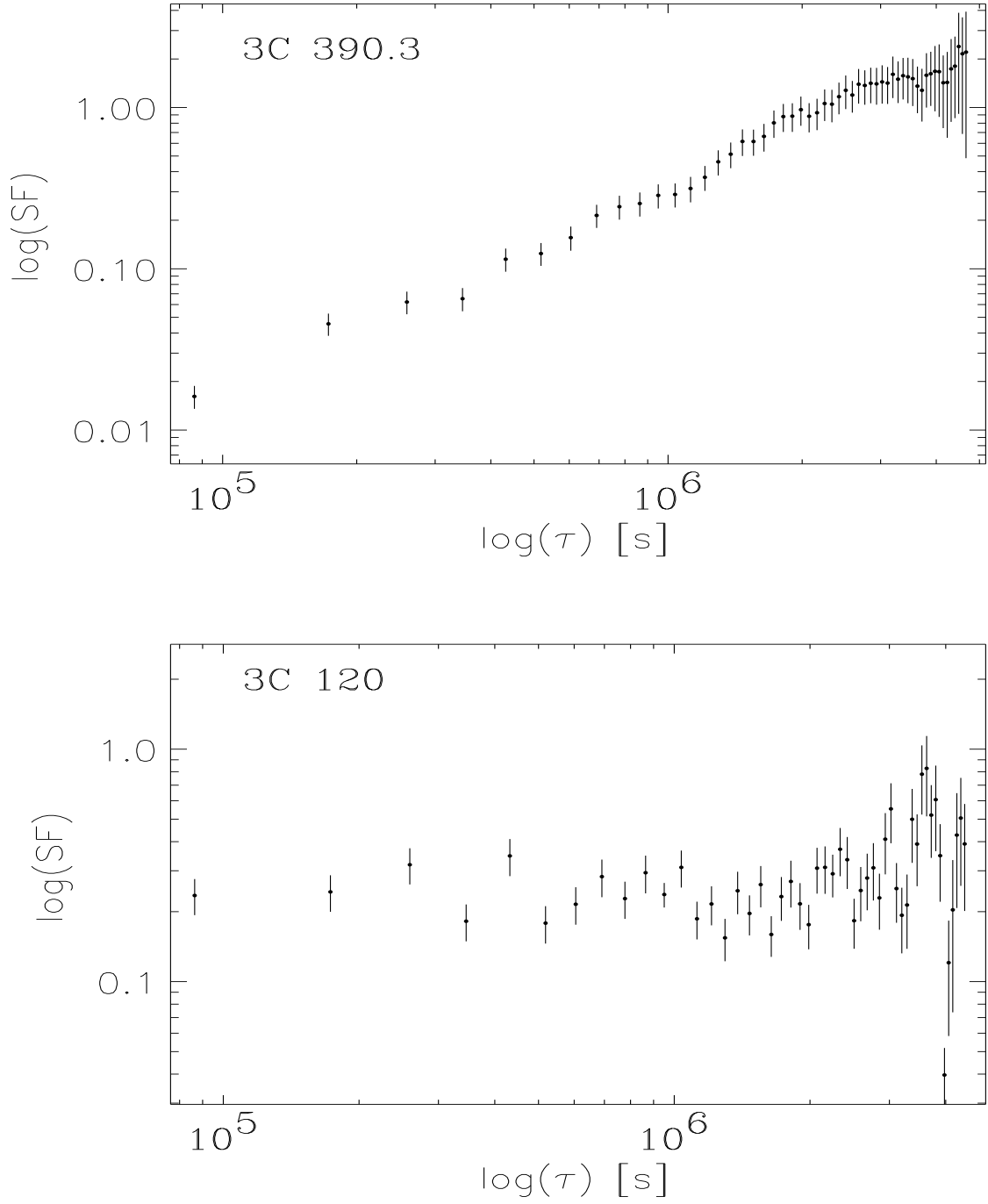


Fig. 2.— Structure functions of 3C 390.3 (top panel) and 3C 120 (bottom panel).

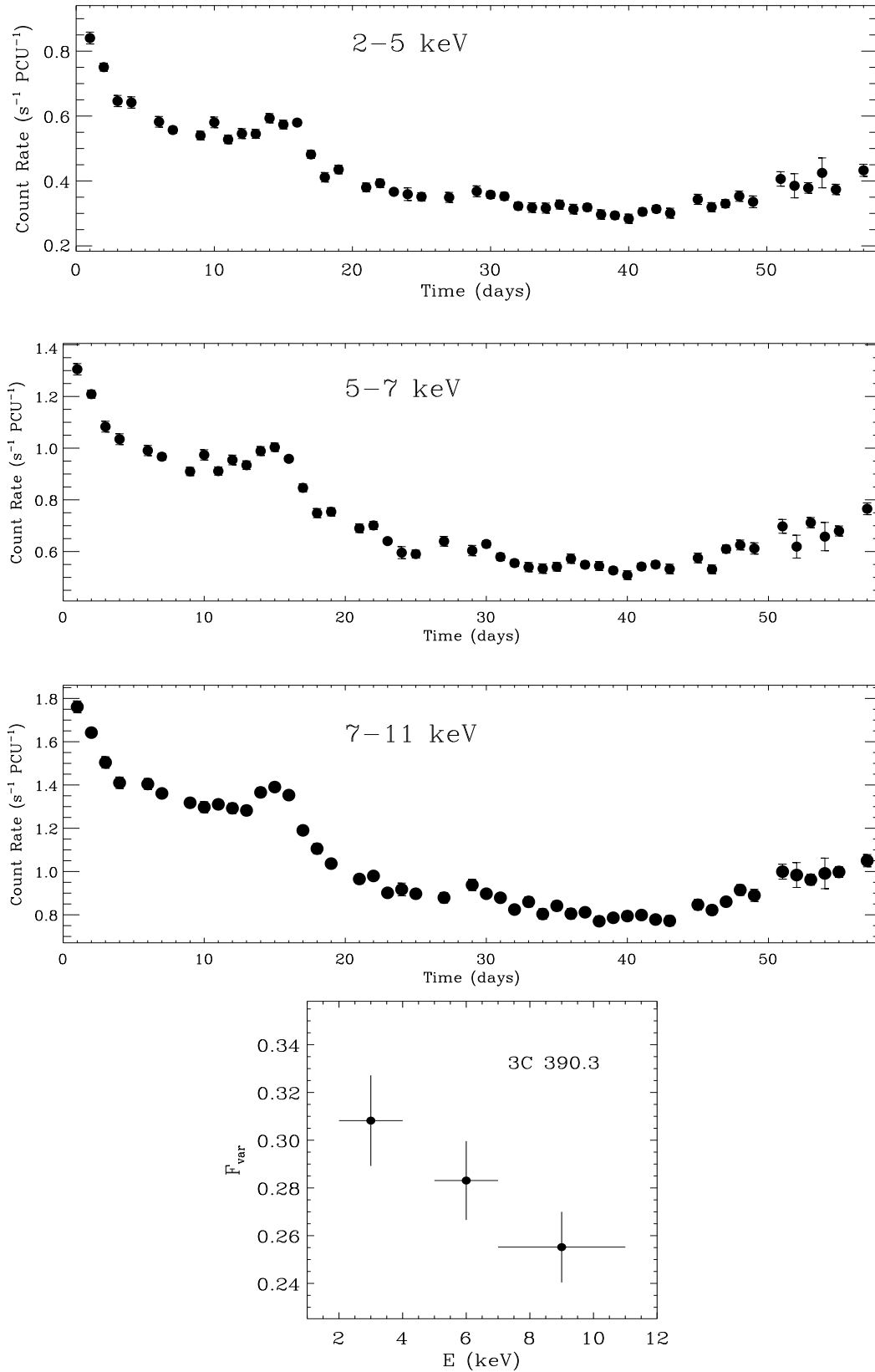


Fig. 3.— X-ray light curves of 3C 390.3 from *RXTE* PCA observations in (top to bottom) the 2-5 keV, 5-7 keV, 7-11 keV bands. Time bins are 5760 s (\sim one *RXTE* orbit). The bottom plot shows the fractional variability parameter versus the energy.

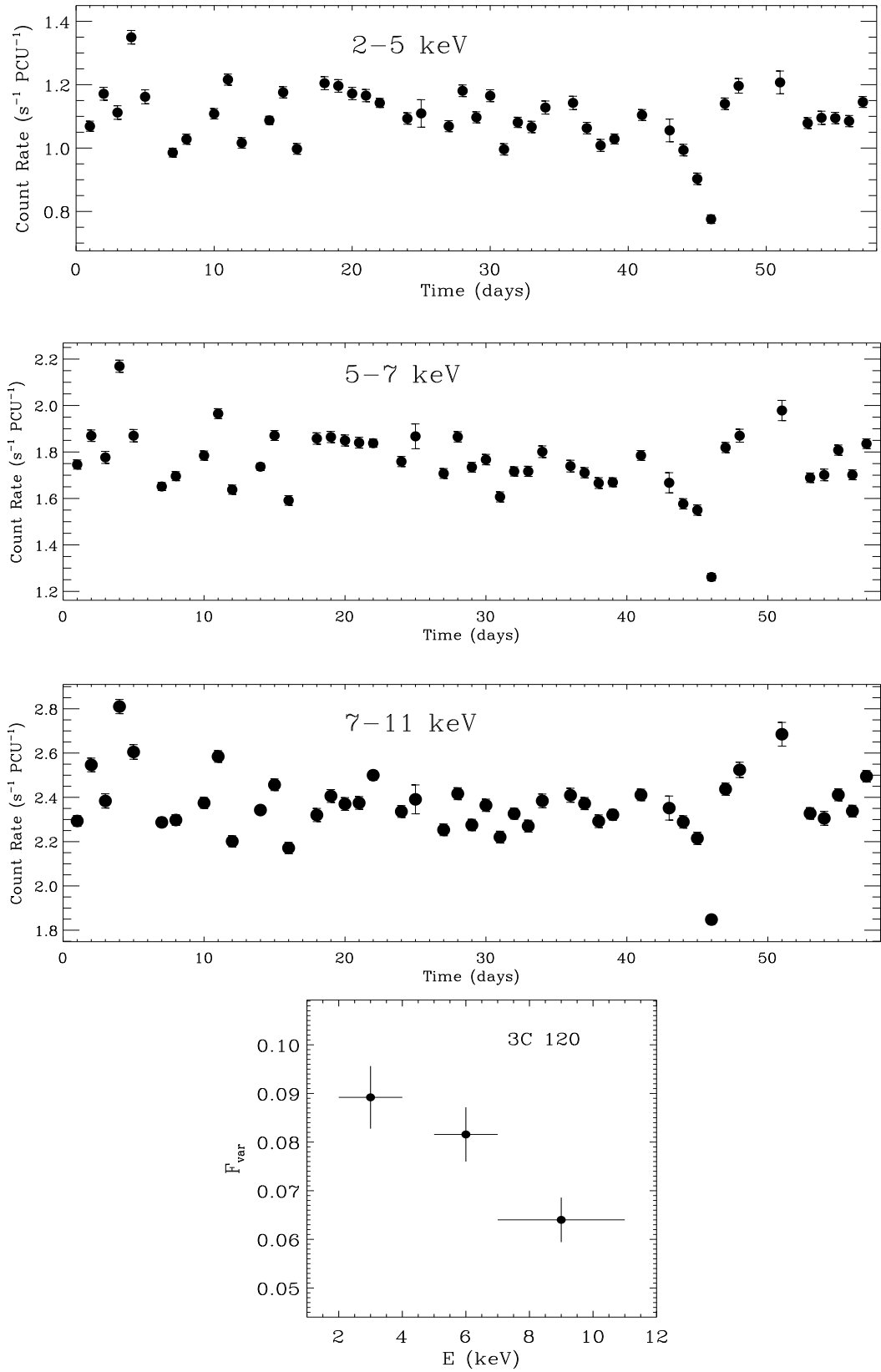


Fig. 4.— X-ray light curves of 3C 120 from *RXTE* PCA observations in (top to bottom) the 2-5 keV, 5-7 keV, 7-11 keV bands. Time bins are 5760 s (\sim one orbit). The bottom plot shows the fractional variability parameter versus the energy.

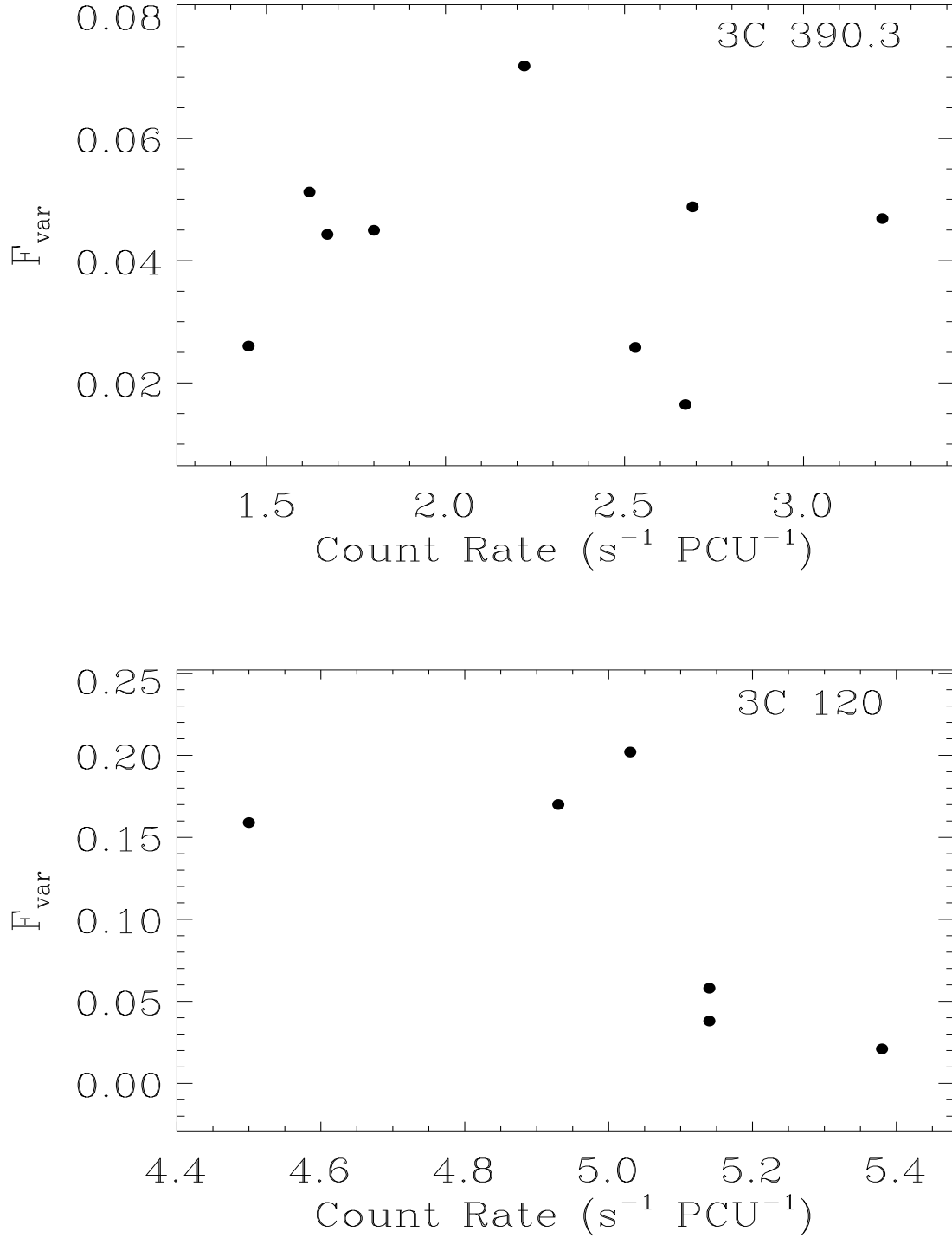


Fig. 5.— F_{var} versus the 2–11 keV count rate, for 3C 390.3 (top panel) and 3C 120 (bottom panel). Time bins are approximately equal to one *RXTE* orbit. The error bars are smaller than the symbol size.

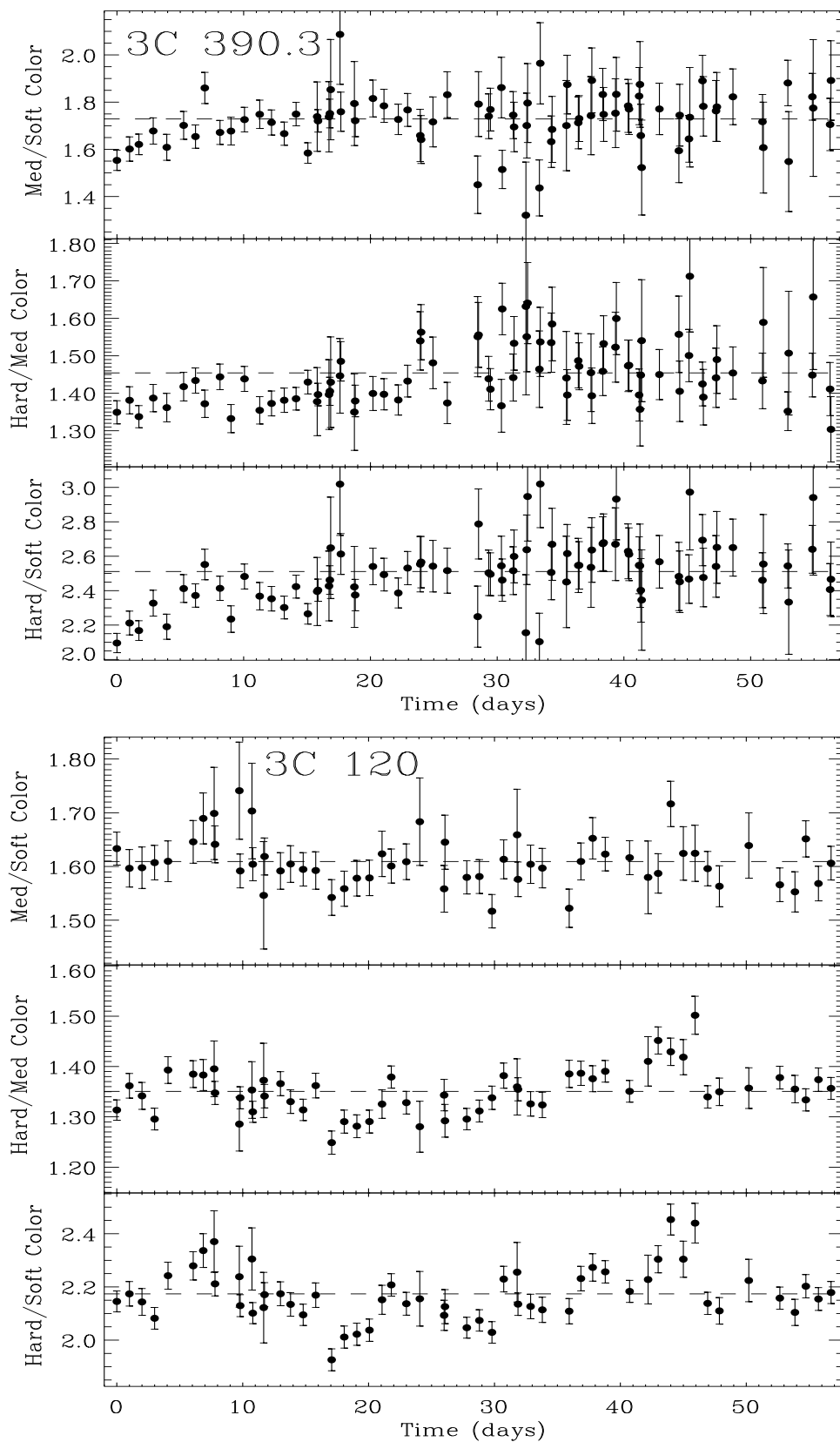


Fig. 6.— Hardness ratio light curve for 3C 390.3 (top panel) and 3C 120 (bottom panel). Time bins are 5760 s (\sim one *RXTE* orbit).

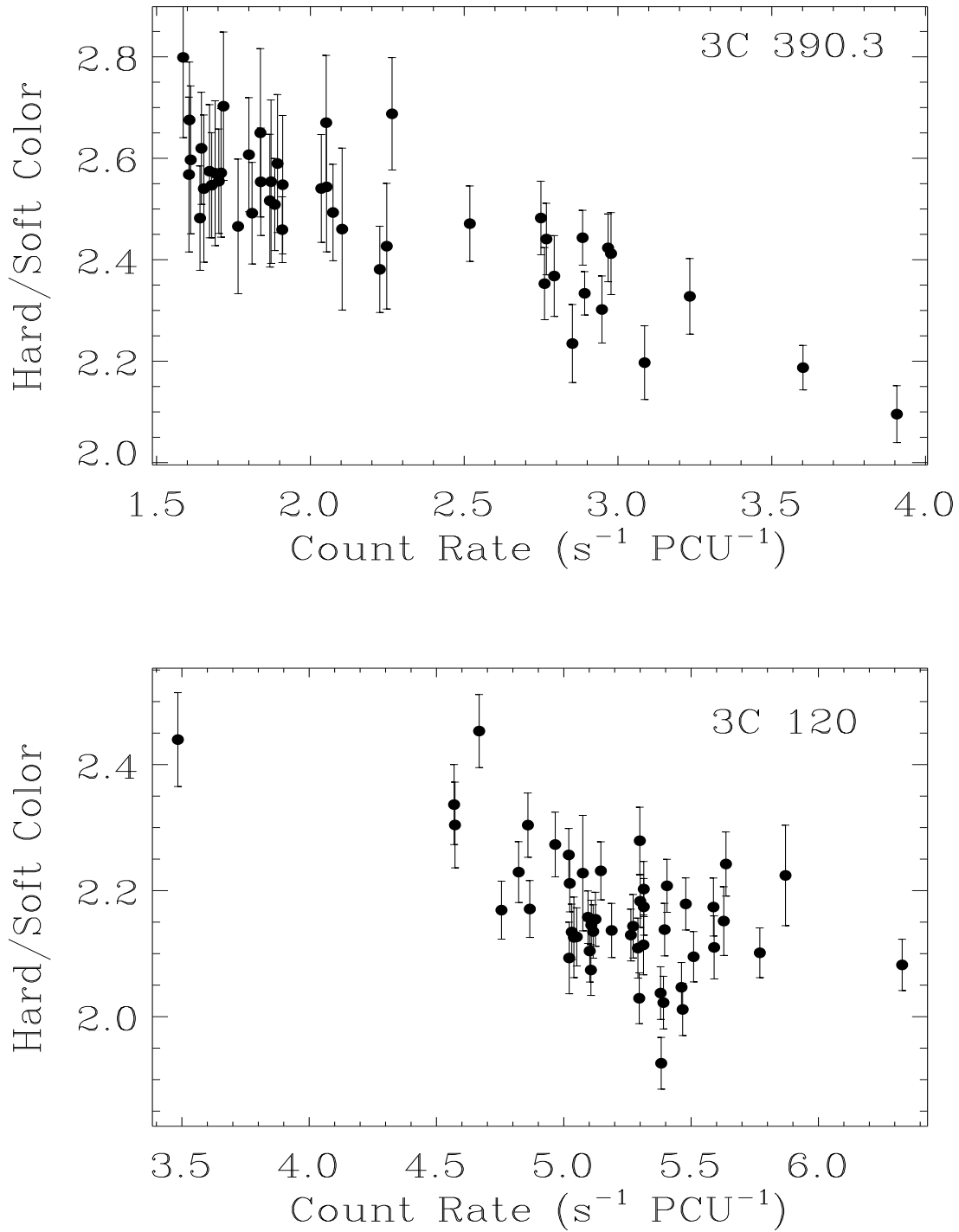


Fig. 7.— Hard/Soft of 3C 390.3 (top) 3C 120 (bottom panel) plotted against the 2–11 keV count rate. Time bins are \sim one orbit.

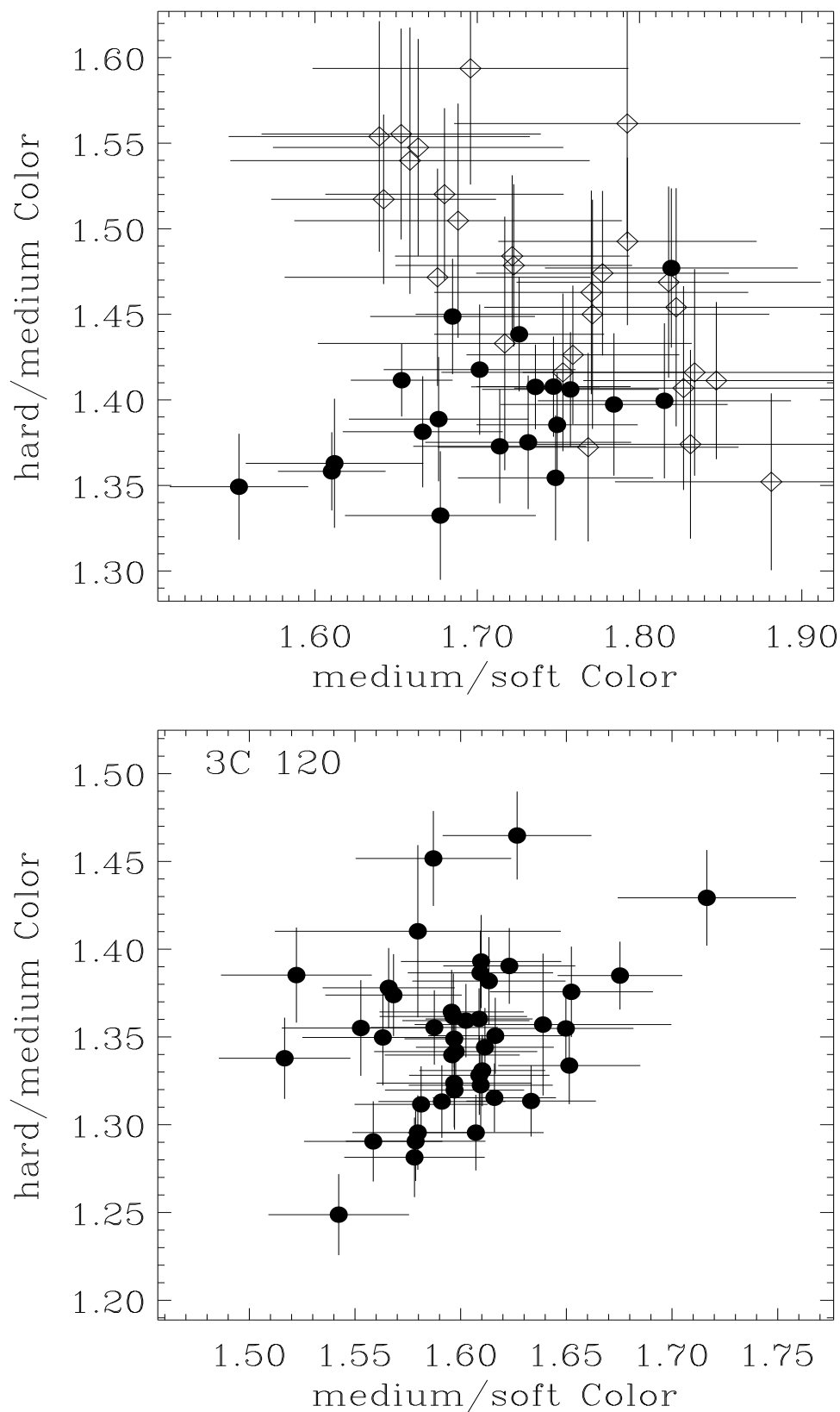


Fig. 8.— Color-color diagrams for 3C 390.3 (top panel) and 3C 120 (bottom panel). Time bins are 1 day. Filled dots refers to the first half of the 3C 390.3 light curve and the open diamonds to the second half.

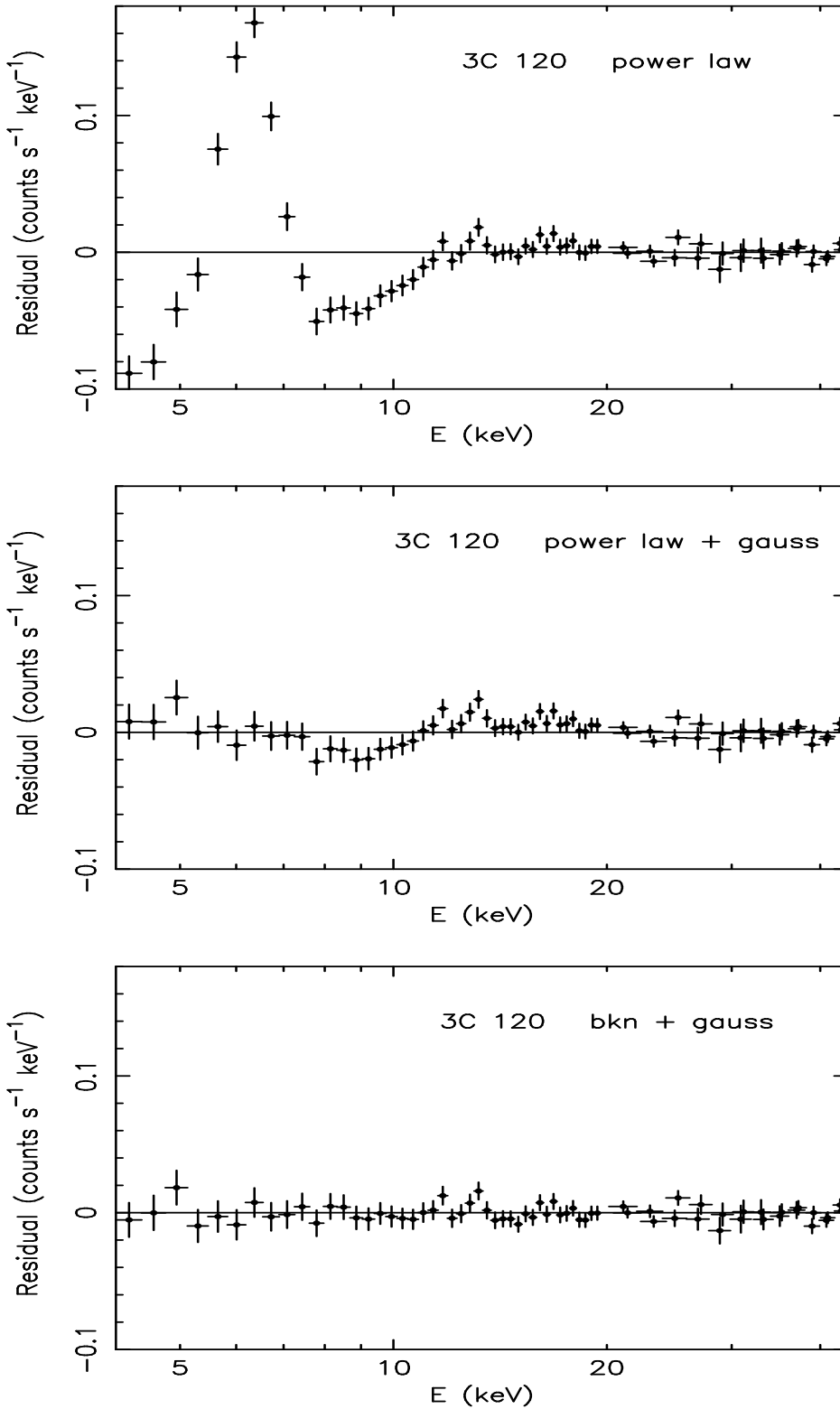


Fig. 9.— Spectral fit residuals to the PCA+HEXTE spectrum of 3C 120 for simple power law (top panel), a power law plus a Gaussian component at 6.4 keV (middle panel), a broken power law plus a Gaussian line at 6.4 keV (bottom panel).

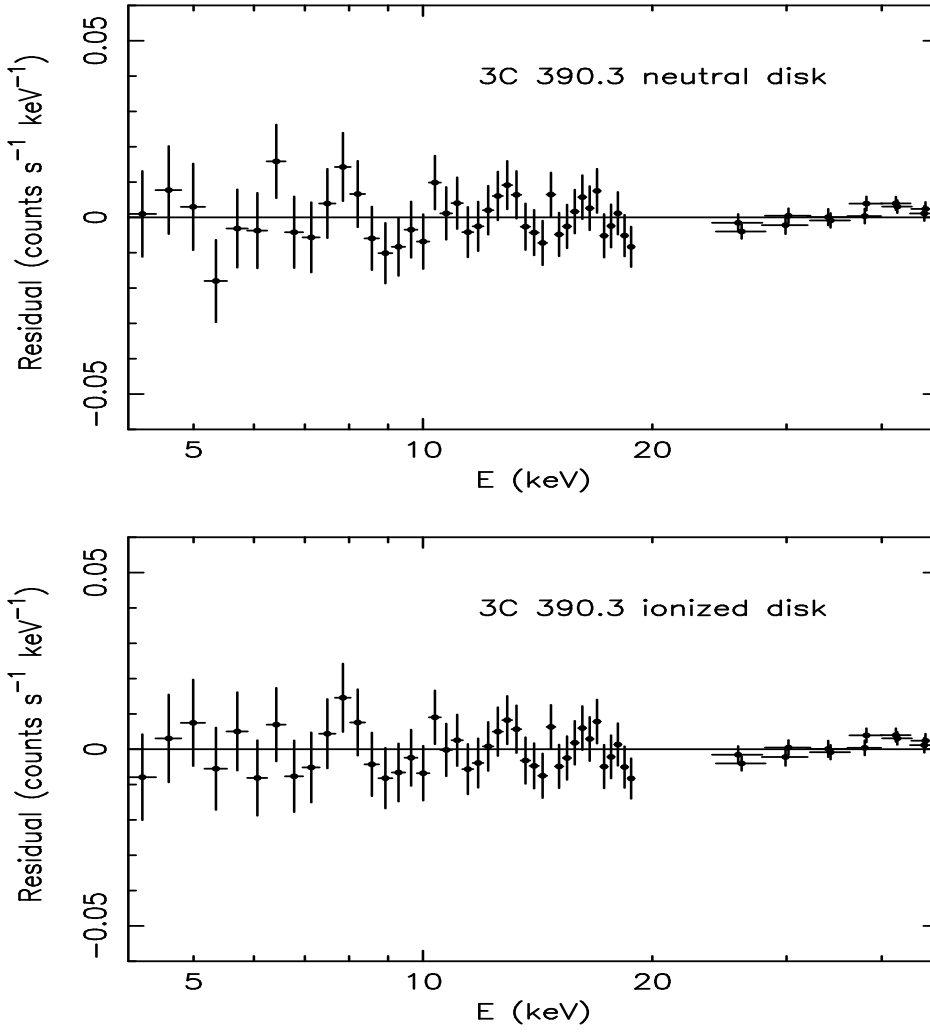


Fig. 10.— Spectral fit residuals to the PCA+HEXTE spectrum of 3C 390.3 for the *pexrav* model (top panel), and for the constant-density ionized-disk model (bottom panel).

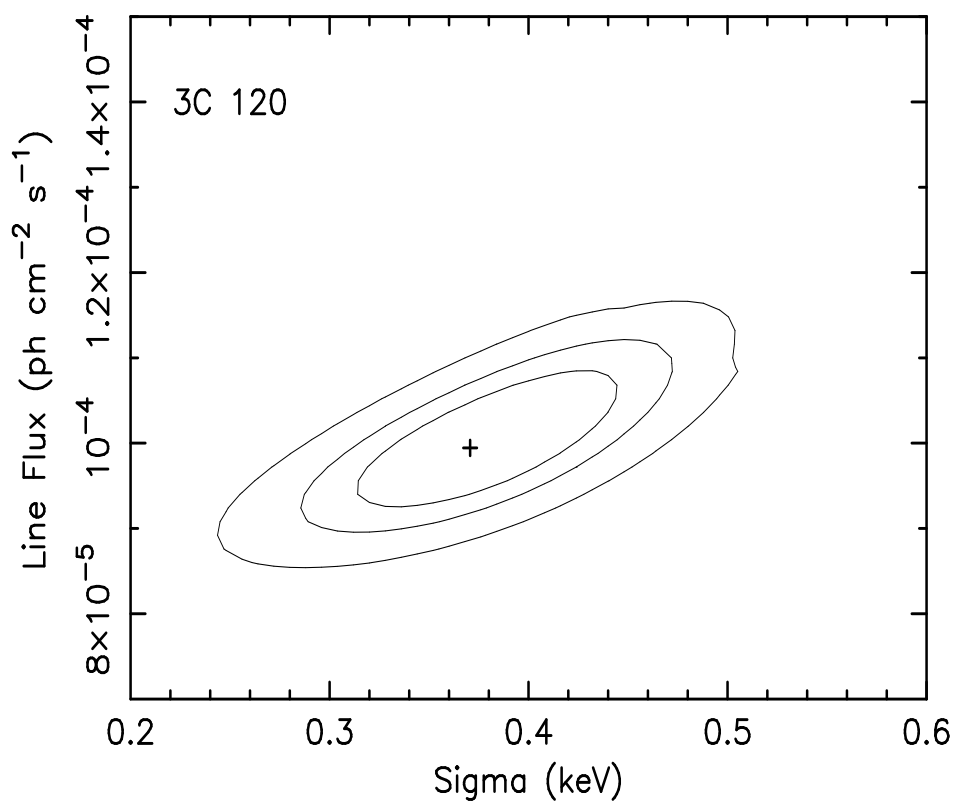
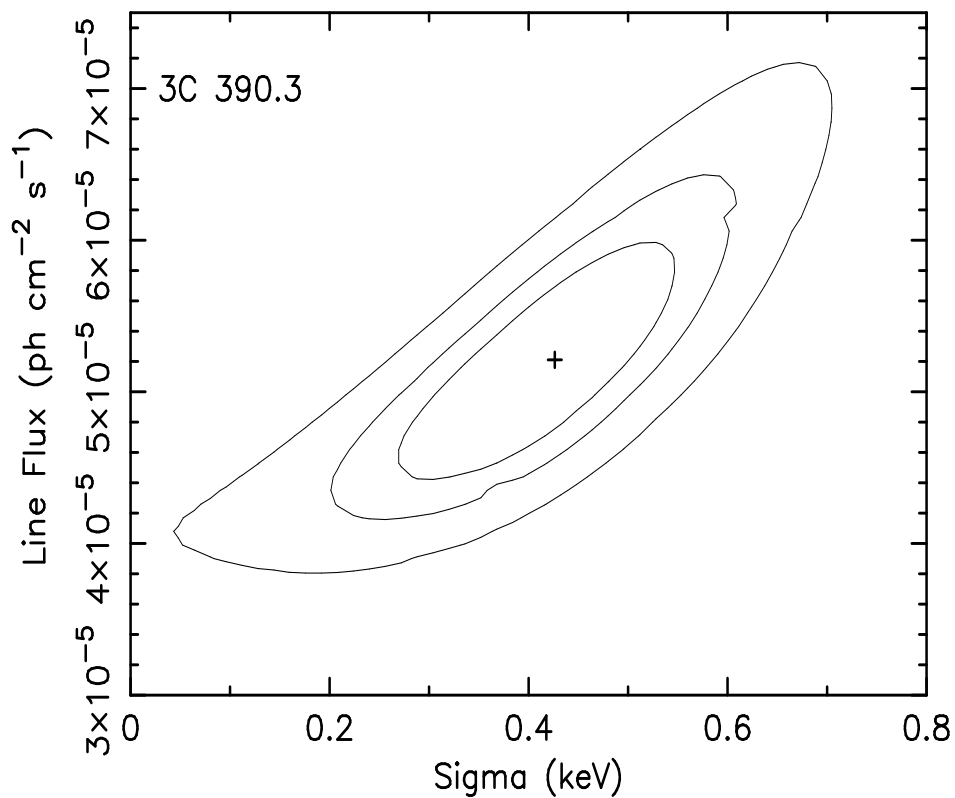


Fig. 11.— Confidence contours (68%,90%, and 99%) in the $\sigma - I_{\text{FeK}\alpha}$ plane. The EW of the line is directly proportional to its photon flux. The conversion factor can be derived from the best-fitting model parameters in Table 5.

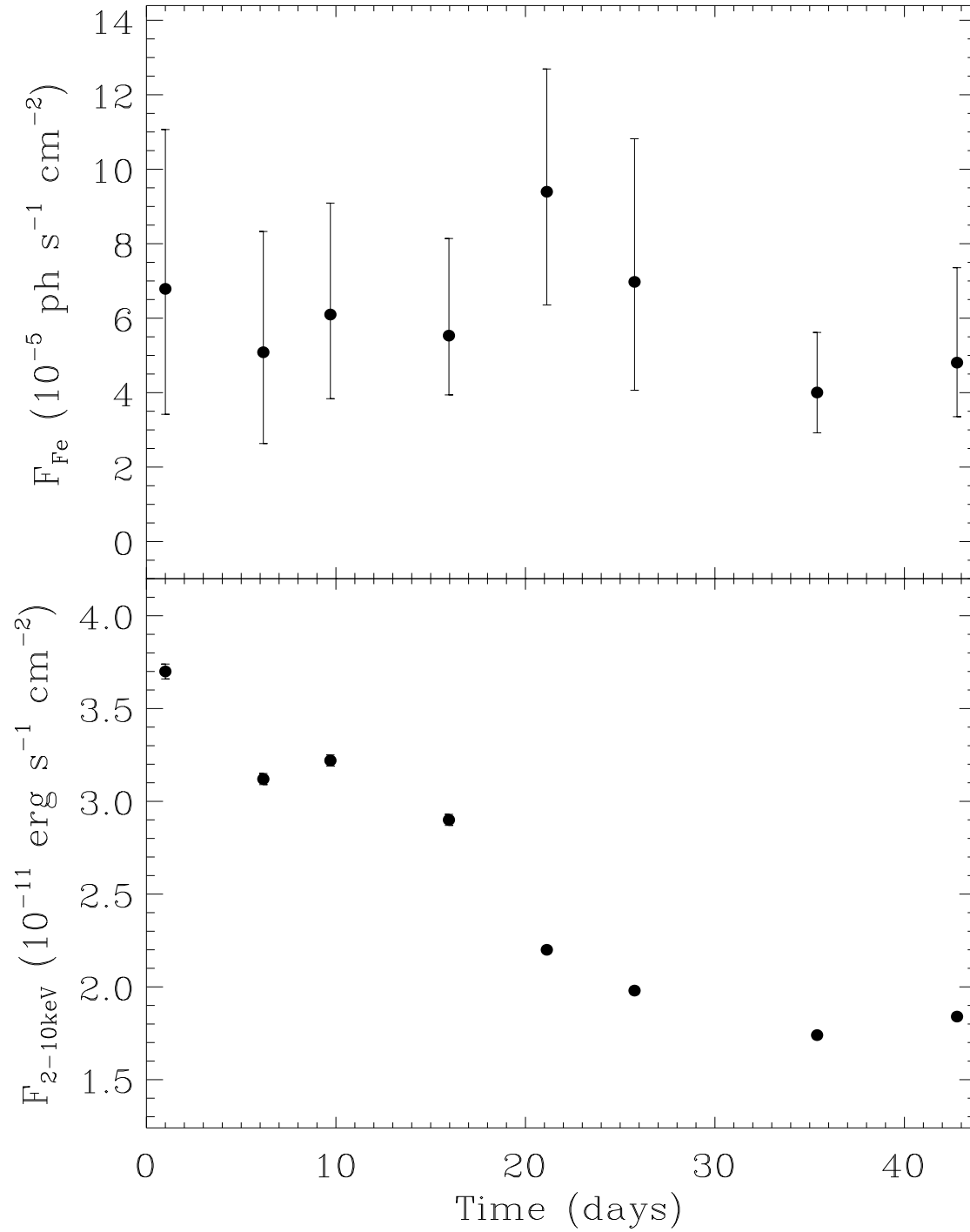


Fig. 12.— Light curves of the Fe K α line flux (10^{-5} photons s $^{-1}$ cm $^{-2}$; top panel) and of the 2–10 keV flux (10^{-11} erg s $^{-1}$ cm $^{-2}$; bottom panel). The error bars correspond to 90% confidence level.

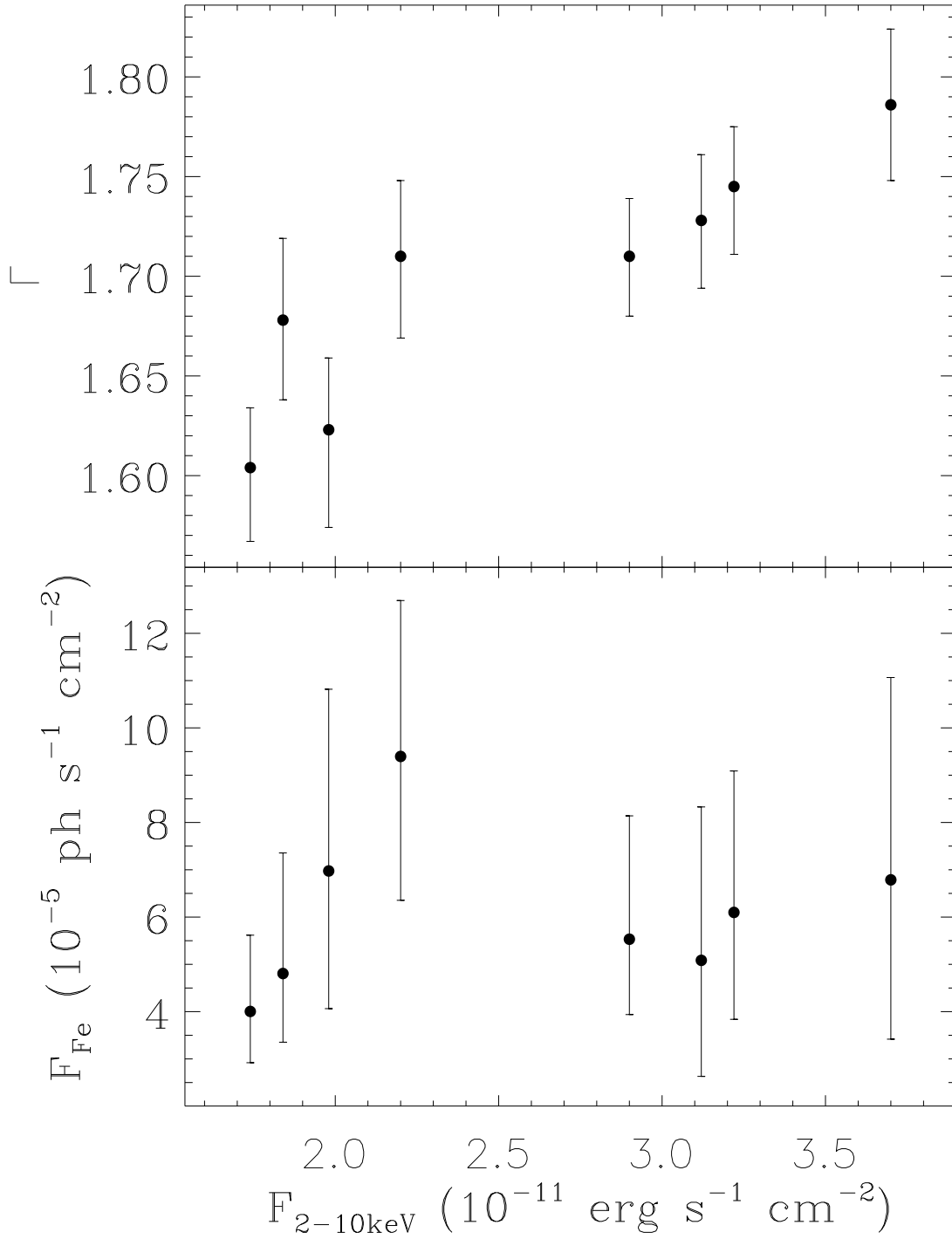


Fig. 13.— Photon index Γ in the range 4-20 keV (top panel) and Fe K α line flux ($10^{-5} \text{ photons s}^{-1} \text{ cm}^{-2}$; bottom panel) plotted against the 2-10 keV flux ($10^{-11} \text{ erg s}^{-1} \text{ cm}^{-2}$).